

Journal Pre-proof

Defining the activity of pro-reparative extracellular vesicles in wound healing based on miRNA payloads and cell type-specific lineage mapping

Dong Jun Park, Wooil Choi, Sakeef Sayeed, Robert A. Dorschner, Joseph Rainaldi, Kayla Ho, Jenny Kezios, John P. Nolan, Prashant Mali, Todd Costantini, Brian P. Eliceiri

PII: S1525-0016(24)00088-1

DOI: <https://doi.org/10.1016/j.ymthe.2024.02.019>

Reference: YMTHE 6327

To appear in: *Molecular Therapy*

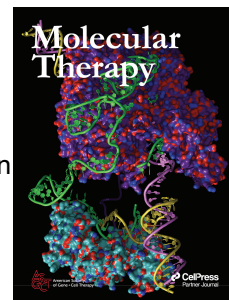
Received Date: 12 September 2023

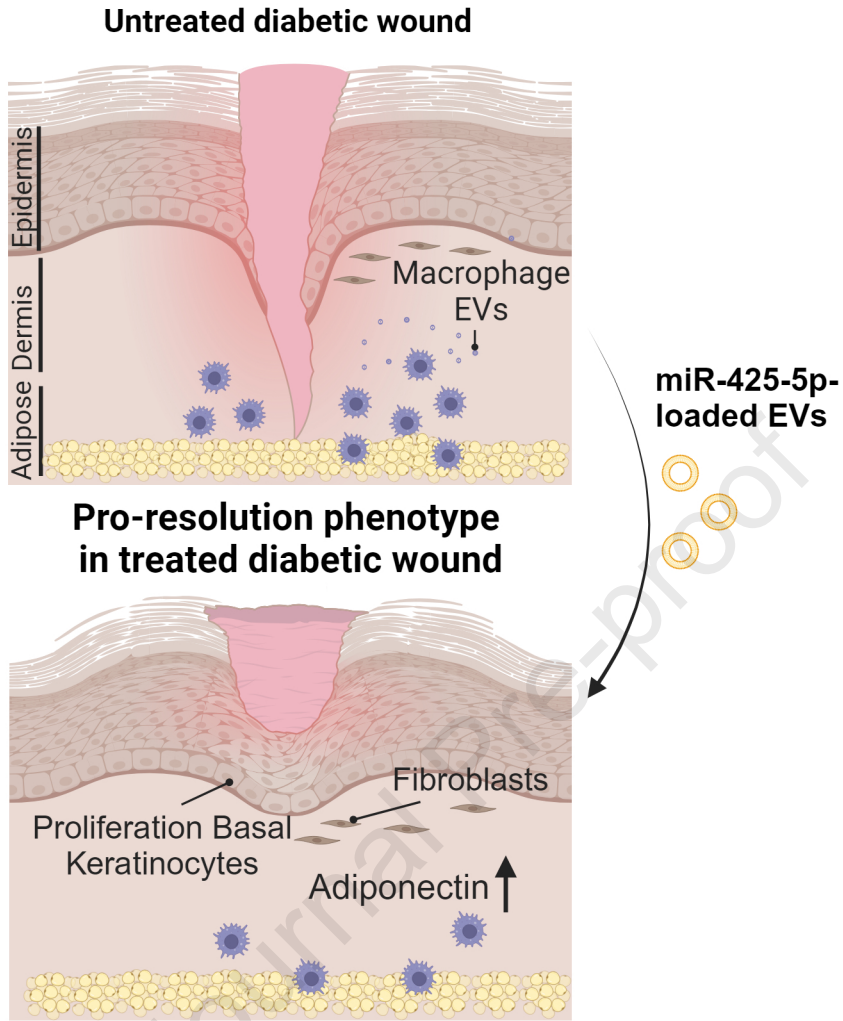
Accepted Date: 15 February 2024

Please cite this article as: Park DJ, Choi W, Sayeed S, Dorschner RA, Rainaldi J, Ho K, Kezios J, Nolan JP, Mali P, Costantini T, Eliceiri BP, Defining the activity of pro-reparative extracellular vesicles in wound healing based on miRNA payloads and cell type-specific lineage mapping, *Molecular Therapy* (2024), doi: <https://doi.org/10.1016/j.ymthe.2024.02.019>.

This is a PDF file of an article that has undergone enhancements after acceptance, such as the addition of a cover page and metadata, and formatting for readability, but it is not yet the definitive version of record. This version will undergo additional copyediting, typesetting and review before it is published in its final form, but we are providing this version to give early visibility of the article. Please note that, during the production process, errors may be discovered which could affect the content, and all legal disclaimers that apply to the journal pertain.

© 2024





1
2
3
4
5
6
7
8
9
10
11
12
13
14
15
16
17
18
19

Defining the activity of pro-reparative extracellular vesicles in wound healing based on miRNA payloads and cell type-specific lineage mapping

Dong Jun Park¹, Wooil Choi¹, Sakeef Sayeed¹, Robert A. Dorschner², Joseph Rainaldi³, Kayla Ho¹, Jenny Kezios¹, John P. Nolan⁴, Prashant Mali³, Todd Costantini¹, Brian P. Eliceiri^{1,2*}

¹Department of Surgery, University of California San Diego, La Jolla, CA 92093, USA

²Department of Dermatology, University of California San Diego, La Jolla, CA 92093, USA

³Department of Bioengineering, University of California San Diego, La Jolla, CA 92093, USA

⁴Scintillon Institute, San Diego, CA 92121, USA

*Correspondence: beliceiri@health.ucsd.edu (B.P.E.)

20 **ABSTRACT**

21 Small extracellular vesicles (EVs) are released by cells and deliver biologically active payloads to coordinate the response
22 of multiple cell types in cutaneous wound healing. Here we used a cutaneous injury model as a donor of pro-reparative
23 EVs to treat recipient diabetic obese mice, a model of impaired wound healing. We established a functional screen for
24 miRNAs that increased the pro-reparative activity of EVs and identified a down-regulation of miR-425-5p in EVs *in vivo*
25 and *in vitro* associated with the regulation of adiponectin. We tested a cell type-specific reporter of a tetraspanin CD9
26 fusion with GFP to lineage map the release of EVs from macrophages in the wound bed, based on the expression of miR-
27 425-5p in macrophage-derived EVs and the abundance of macrophages in EV donor sites. Analysis of different
28 promoters demonstrated that EV release under the control of a macrophage-specific promoter was most abundant and
29 that these EVs were internalized by dermal fibroblasts. These findings suggested that pro-reparative EVs deliver
30 miRNAs such as miR-425-5p that stimulate the expression of adiponectin that has insulin-sensitizing properties. We
31 propose that EVs promote intercellular signaling between cell layers in the skin to resolve inflammation, induce
32 proliferation of basal keratinocytes, and accelerate wound closure.

33

34 INTRODUCTION

35 Healthy repair of cutaneous wounds is a coordinated response of hemostasis, immune cell recruitment,
36 angiogenesis, and re-epithelialization,^{1,2} however, dysregulation of these normal processes in diabetes, obesity, aging
37 and infection presents a risk for chronic wounds.^{3,4} Recent studies have identified extracellular vesicles (EVs), especially
38 small EVs (50-120 nm), as the most abundant EV mediators of signaling crosstalk between mammalian cells.⁵⁻⁷ In the
39 context of wound healing, we have previously shown that small EVs comprise the vast majority of all EVs in the wound
40 bed,⁸⁻¹⁰ and deliver biologically active nucleic acid and protein payloads demonstrating their physiological relevance in
41 intercellular signaling in skin injury.^{8,11} Currently, many EV studies include the use of *in vitro* cultured cells as EV
42 donors that often test activity of human cell-derived EVs in mouse models.¹² The use of human derived EVs in mouse
43 models represents a significant limitation of the translational potential because of rejection considerations. An additional
44 limitation is the overall lack of *in vivo* studies that address the heterogeneity of *in vivo* EV donors and the cell type of
45 origin of EVs released into the wound microenvironment.^{11,13,14}

46 Since pro-reparative activity of EVs that is generally associated with their ability to promote tissue repair by
47 horizontal transfer of nucleic acids and proteins to recipient cells,^{7,15} we developed an allograft model where EVs were
48 harvested from subcutaneous implantations of sterile polyvinyl alcohol (PVA) sponges.^{9,10} PVA sponge implants were
49 originally developed as an animal model of foreign body response that we adapted for the efficient recovery of cells that
50 release EVs relevant to the immune component of the injury response and for *in vivo* gene delivery to modify the activity
51 of infiltrating cells.¹⁶⁻¹⁸ The key advantages are that high concentrations of biologically active EVs are recovered using
52 non-destructive approaches without the complications of blood products and culture media components used *in vitro*.⁸
53 We previously used this model to identify the mobilization of human myeloid cells to PVA sponge implants in humanized
54 mouse models, defined the activity of specific EV biogenesis genes that uncouple the production of pro-reparative EVs
55 in wound healing, and used vesicle flow cytometry (vFC) to quantify EV heterogeneity *in vivo*.^{9,10} Another key limitation
56 of many wound healing studies of EVs as therapeutics is the lack of translationally relevant animal models of impaired
57 tissue repair. We addressed this by focusing on testing of genetically-defined mouse models of impaired wound healing
58 such as the Leptin receptor knockout mouse, referred to as the db/db mouse, that has an onset of obesity and
59 hyperglycemia at 12 weeks of age.¹⁹⁻²² db/db mice are characterized by impaired wound healing kinetics and are an
60 important genetic model for the study of injury-related complications in diabetes. Protease inhibitors were identified as

61 down-regulated in EVs isolated from db/db mice. In the context of functional testing of the biological activity of specific
62 pro-reparative EV payloads, we have recently engineered the protein payload of the EVs. Specific protease inhibitors
63 were over-expressed in engineered EVs and used to reverse the impaired wound healing phenotype.⁸ Together, we
64 identified the importance of using genetically-defined donor mice for allograft studies of the biological activity of donor
65 EVs to address a major challenge in the translational relevance of EVs as therapeutics and engineered EV payloads in
66 cutaneous injury.

67 While the relative importance of EVs released from various cell types *in vivo* remains poorly understood, recent
68 advances in the development of cell type-specific transgenic models have demonstrated the utility of tracking fluorescent
69 EV reporters.²³⁻²⁶ For example, expression of EV-associated proteins such as the tetraspanins CD9, CD63 and CD81 as
70 fusion proteins with fluorescent reporter proteins can be used to identify EV distribution in the circulation and tumor
71 microenvironment. Since these three tetraspanins are among the most highly enriched EV markers, they have been used
72 to monitor EV trafficking *in vitro* in release and uptake studies.^{25,26} In the context of cutaneous injury and our
73 development of defined allograft models of EV release,⁸⁻¹⁰ we used single cell RNA sequencing (scRNAseq) to define
74 the cellular landscape from where EVs are harvested in combination with transgenic mice expressing CD9 with a C-
75 terminal green fluorescent protein (GFP) tag to determine the relative contributions of specific cell types in the donor
76 site microenvironment.²⁴ These reporter approaches address key questions regarding the relative contributions of EVs
77 released from different cell types, as well as being useful tools to assess the uptake of GFP⁺ EV populations in recipient
78 cells. In addition to GFP-based reporter models, we used single vFC to quantify the size, number, expression of specific
79 endogenous proteins presents on the surface of EVs, as well as tracking of epitope tagged EV proteins.

80 In the field of cutaneous injury, intercellular communication can regulate differentiation and tissue injury
81 responses between adipose, dermal, and epidermal cell layers. Directional movement of cells can also be controlled by
82 persistent release of EVs that conditions the microenvironment, promotes adhesion, and regulates cell polarization.²⁵
83 Therefore, we focused on testing the pro-reparative activity of EVs isolated from wildtype (WT) vs. db/db animals
84 implanted with PVA sponges that were used to collect donor site EVs. We identified EV-mediated differences in EVs
85 from WT vs. db/db donors that regulated wound repair kinetics, changes in microRNA (miRNA) payloads and tested the

86 activity of specific miRNAs by loading EVs and testing their capacity to restore tissue repair in the impaired wound
87 healing model db/db recipient mice.¹³

88 Together, these studies take advantage of recent technological advances in vFC,²⁷ EV payload profiling by
89 miRNAseq,²⁸ transgenic reporters to identify EV source,²⁹ and uptake in cell types relevant to wound repair.⁶ Based
90 on the distribution of macrophages interspersed in subcutaneous adipose tissue,³⁰ we propose that macrophage-derived
91 EVs can be internalized by overlying fibroblasts, leading to production of adipokines such as adiponectin that are pro-
92 reparative and associated with increased cell proliferation of basal keratinocytes. Our data supports a model in which
93 EV-mediated acceleration of wound closure is regulated by specific miRNA payloads released by donor cells such as
94 macrophages to affect the activity of overlying cell layers of the skin.

95

96 **RESULTS**

97 **Diabetic obese mice drive a transcriptional reprogramming of immune cell subsets recruited into sites of** 98 **cutaneous injury.**

99 To determine the source of EVs and identify biologically active payloads in impaired models of wound healing
100 in the analysis of EVs from biological fluids it was essential to have model systems with defined cell profiles. Therefore,
101 we used scRNAseq to identify the activation state of cell types infiltrating sterile subcutaneous PVA sponges implanted
102 in the dorsum of WT mice (Figure 1A), a model that we and others have shown reflects the recruitment of macrophages
103 and neutrophils observed in wound healing.^{8-10,31} scRNAseq was performed at 7 days post-implantation, a timepoint that
104 we previously showed was associated with peak of EV release,⁸ to identify cells recruited to the PVA sponge. These
105 cells were primarily macrophages and neutrophils, along with lower levels of dendritic cells and lymphocytes, as seen
106 on the UMAP projection (Figure 1B and Supplementary Figures S1A and B). Expression of canonical genes associated
107 with each cell type (Log2Max visualization of multiple genes based on Loupe Browser; Figure 1C and Table S1) were
108 used as the basis to identify cell type-specific changes in gene expression mediated by the loss of the leptin receptor in
109 the db/db mouse model (Figure 1D). Cell type designations were based on canonical genes for each cell type (i.e., *Trem2*
110 for macrophages, *S100a8* for neutrophils, *Ccr7* and *Zbtb46* for DCs, and *CD3* for lymphocytes).³²⁻⁴² Additional genes
111 (i.e., *H2-dmb1* and *Ms4a4c*) were also identified as highly expressed in macrophages infiltrating PVA sponges (Table

112 S1).^{43,44} We identified changes in gene expression that were common among several cell types such as increased levels
113 of Apolipoprotein E (*ApoE*), Cathepsin L (*Ctsl*), and Prostaglandin synthase (*Ptgs2*), and Cystatin domain proteins
114 (*Cstcd4*). Cell type-specific changes in gene expression of the top 10 genes upregulated vs. down-regulated genes of WT
115 vs. db/db PVA sponges were observed in each major cell type. For example, we noted changes of specific genes in
116 macrophages (*Stfa211* and *Trf*), neutrophils (*Egr*), DCs (*Lyz2* and *Ccl17*), and lymphocytes (*Mmp12* and *Il1r2*).
117 scRNAseq analysis identified additional changes in gene expression associated with the db/db mouse model that were
118 primarily comprised of metabolic factors associated with diabetic obesity (Supplementary Figure S1D). Importantly,
119 regardless of the genetic background of the donor mice, similar numbers of macrophages, neutrophils, DCs and
120 lymphocytes were recruited to the PVA sponge in db/db and WT mice (Supplementary Figure S1E and F), and were
121 consistent with analyses of cell types recruited to the PVA sponge based on antibody-dependent flow cytometry studies.⁸
122 These findings identified macrophages and neutrophils as the predominant cell types in the PVA sponge model used as
123 *in vivo* EV donors. In addition, this data showed that although there were differences in the gene profile of cells harvested
124 from WT vs db/db mice, these changes were related to their physiology rather than affecting pathways directly related
125 to EV release.

127 **Characterization of EVs released into biological fluid of cutaneous injury site.**

128 Our previous studies established the efficacy of PVA sponge implants as an *in vivo* source of highly concentrated
129 EVs relevant to wound healing.⁸ We used these established standard parameters to analyze EVs purified from PVA
130 implants in WT and db/db mice. EVs harvested from the PVA sponge implants in the wound fluid were subjected to
131 serial centrifugation followed by size exclusion chromatography (SEC) (Figure 2A). We have previously shown that the
132 most numerous EVs in subcutaneous implants of PVA sponges were 100-120 nm in diameter and comprised the vast
133 majority of all EVs observed in this biological fluid, with relatively few larger EVs being observed.⁸ Each fraction of
134 the SEC was analyzed for EV concentration using vesicle flow cytometry (vFC) as assessed by staining with the
135 fluorescent lipophilic membrane dye, vFRed (Figure 2B, column), and compared in parallel with protein concentration
136 in each fraction (Figure 2B, line) as detailed in the Methods and Materials. Each fraction of the SEC was further validated
137 for EV content by immunoblotting for a canonical EV marker like the tetraspanin CD9. We identified of high levels of
138 CD9 protein in the EV containing fraction 7 by immunoblot (Figure 2C) and by vFC with a fluorescently-labeled anti-

139 CD9 antibody (Supplementary Figure S2). Low levels of CD9 protein were detected in later fractions that lacked
140 significant numbers of small EVs (i.e., fractions 15-20; Figure 2C). Immunoblotting of whole cell lysates (WCL)
141 compared to purified EVs from the same WT PVA sponges demonstrated that CD9, CD63, CD81, and Alix were all
142 expressed in mouse PVA sponge EVs (Figure 2D). Enrichment of CD9 and Alix in EVs vs. WCLs was noted in the
143 analyses of mouse PVA sponge EVs, suggesting that these proteins may be more EV-specific. For the characterization
144 of EVs isolated from db/db mice, we established cohorts of 12–16-week-old WT and db/db mice where db/db mice used
145 for the collection of EVs were significantly more hyperglycemic (Figure 2E) and obese (Figure 2F) compared to WT
146 mice. These two parameters were the hallmark of the diabetic obese phenotype that is characteristic of the db/db mouse
147 model. The concentration of EVs isolated from PVA sponges was in the range of $5\text{--}7 \times 10^6$ PVA EVs/ μL (Figure 2G).
148 EVs isolated from WT and db/db mice had similar size distributions with the mean diameter of EVs detected being 116.7
149 ± 8.79 nm ($n=6$) from db/db donors and 119.8 ± 6.8 nm ($n= 6$) from WT donors (Figure 2H). Similar sizing analysis of
150 each of the other SEC fractions did not reveal any substantial numbers of larger EVs in later fractions (Figure 2B and
151 data not shown). Transmission electron microscopy established that the EVs purified from WT and db/db donors had a
152 similar size and shape (Supplementary Figure S3A). To monitor for the potential of lipoprotein contamination of EV
153 fractions collected by SEC we performed immunoblotting of SEC fractions with an antibody to detect lipoproteins such
154 ApoE that could be present in EV fractions. We confirmed that the EVs collected in early fractions of the SEC (i.e.,
155 fractions 6-9; See Figure 2B) were well-separated from lipoproteins observed collected in late fractions (i.e., fractions
156 21-23; Supplementary Figure S3B and C). We also observed that the levels of ApoE expression were unchanged between
157 WT and db/db EVs (Supplementary Figure S3D).^{45,46} Together, these analyses established the purification, expression
158 of canonical protein markers, size, and concentration from an *in vivo* EV donor model that is known to exhibit a well-
159 defined phenotype of impaired wound healing.⁸

161 **Identification of changes in EV proteins isolated from diabetic obese donor model.**

162 To determine the profile of proteins expressed on the EV surface we used a combination of batch and single EV
163 analysis (i.e., vFC; Figure 3A). WT EVs were purified from cutaneous implants and subjected to a multiplex analysis
164 (Figure 3B) that identified proteins associated with leukocytes (i.e., CD45, MHCII, and CD20), leukocyte activation
165 (CD44, CD66a) and cell adhesion (CD49e, CD11b, CD61). To address the heterogeneity of EVs in this biological fluid,

166 we performed vFC to determine the expression of individual tetraspanins that are generally used as EV markers. We
167 observed high levels of CD9 and CD63 expression on the surface of WT EVs (Figure 3C). Further, vFC analysis
168 identified several immune cell-relevant proteins expressed on the surface of WT EVs such as MHC I, CD29 (ITGB1),
169 CD274 (PD-L1), and CD39 (ENTPD1) (Figure 3D). These assays on WT EVs formed the basis for the vFC analysis of
170 proteins expressed on biological replicates of WT vs db/db EVs (n=5 for each genotype). For example, we observed that
171 expression levels of tetraspanins CD9 and CD63 measured by vFC were unchanged between WT and db/db EVs thus
172 providing a control for the levels of EVs collected from each genotype using canonical tetraspanin markers (Figure 3E).
173 Based on the importance of integrins in mediating binding to the extracellular matrix, we next measured proteins levels
174 of integrins by vFC. We noted reductions of in the number of EVs expressing detectable CD11b (ITGAM) (0.6-fold
175 decrease, $p < 0.0026$) and CD49e (ITGA5) (0.69-fold decrease, $p < 0.0074$) in db/db vs. WT EVs, but no significant
176 change for CD29 (ITGB1) (Figure 3F). We observed significant reductions in the number of EVs expressing detectable
177 immune-related proteins CD45 (PTPRC) (0.77-fold decrease, $p < 0.0285$), CD44 (hyaluronic acid receptor) (0.83-fold
178 decrease, $p < 0.0246$), and CD54 (ICAM1) (0.75-fold decrease, $p < 0.0221$). In contrast, levels of CD274 (PD-L1) were
179 increased in db/db vs WT EVs (1.47-fold increase, $p < 0.0345$). Levels of MHC I-positive EVs were unchanged (Figure
180 3G). We observed no significant changes in the number of EVs positive for other EV markers implicated in injury
181 models including CD326 (EPCAM), CD39 (ENTPD1), CD66a (CEACAM1), CD24 (HAS), or CD126 (IL6R) (Figure
182 3H).⁴⁷⁻⁵¹ Taken together, these findings suggested that the quantitative differences in the expression of select integrins
183 and other immune-related factors between WT and db/db EV donors may affect EV binding and activity in the wound
184 bed.

185 186 **EVs from diabetic obese donors have impaired wound healing activity.**

187 We previously reported that the pro-reparative phenotype of EVs in wound healing can be uncoupled by
188 interference with specific EV biogenesis pathways,⁹ and that the EV profile (i.e., expression of proteins on the surface
189 of EVs) is regulated by the genetic background of immune-deficient and db/db donor models.¹⁰ To define the activity of
190 EVs from db/db vs. WT donors, we purified EVs from PVA sponge implants from WT and db/db mice as described
191 above and applied these EVs to naïve wounds (Figure 4A). Specifically, EVs were applied topically in a single dose (5-
192 10×10^6 EVs/50 μ l/wound) to freshly prepared splinted full thickness wounds into naive recipient db/db mice, the standard

193 mouse model for impaired wound healing (Figure 4B). We observed that db/db donor EVs had a significant reduction
194 of pro-reparative activity in wound healing compared to the treatment with WT control EVs at Days 5, 7, 10 and 13
195 (n=10; Figure 4C, p values: **<0.005, *<0.05). Analysis of the kinetics of db/db EV-mediated wound closure was
196 comparable to saline-treated controls (Figure 4C). Histological analysis revealed decreases in wound closure (Figure
197 4D), and statistically significant reductions in epidermal thickness (Figure 4E; p <0.0001), and dermal cellularity in the
198 margins (Figure 4F; refer to brackets in Figure 4D for regions of analysis; p <0.0001) of wounds treated with db/db vs.
199 WT EVs. To determine whether there were differences in epithelial cell proliferation in EV-treated wounds, a hallmark
200 of the wound repair process,^{52,53} we performed immunostaining with an anti-Ki67 antibody to localize the effects of EVs
201 on proliferation. We observed that treatment with WT EVs promoted proliferation of basal keratinocytes as detected by
202 the increase in Ki-67⁺ cells, a molecular endpoint that is physiologically relevant for wound closure, whereas there was
203 an absence of Ki67⁺ cells in basal keratinocytes of db/db EV-treated wounds was observed (Figure 4G). Given this effect
204 of WT EV treatment stimulating the proliferation of basal keratinocytes, we focused on an EV tagging strategy to assess
205 the distribution of EVs in the wound bed to better understand what cells may uptake EVs based on localization of the
206 EV tag. We designed a FLAG-tagged tetraspanin CD63 that would express the FLAG tag on the outside of the EV that
207 took advantage of the transient transfection properties of a cell line like HEK293 to rapidly prepare high purity EVs for
208 biological testing. Since HEK293 cells are also widely used in the EV field for engineering and production,⁵⁴⁻⁵⁶ we could
209 purify EVs from the conditioned media of cultured HEK293 cells that either over-expressed human CD63 or CD63-
210 FLAG (Figure 4H, top). We determined that the FLAG epitope was displayed on 29% of all EVs collected from the
211 conditioned media (Figure 4H, bottom). FLAG expression was confirmed by immunoblotting of EVs from CD63-FLAG
212 transfected cells vs. control CD63-transfected cells (Figure 4I). Next, CD63-FLAG or CD63 expressing EVs were added
213 to full thickness wounds and incubated for 24 hours. Upon harvest and immunohistochemical staining to detect the
214 FLAG tag, we observed uptake of FLAG-tagged EVs in cells of the dermis, where especially in the higher
215 magnifications, FLAG-positive cells were observed primarily in the dermis, a cell layer characterized by an abundance
216 of fibroblasts (Figure 4J). Wounds treated with untagged CD63 or saline treated wounds used as negative
217 immunohistochemical controls (Figure 4J). Based on the substantial localization of FLAG-tagged EVs in the dermis,
218 we further assessed the uptake of CD63-FLAG-expressing EVs into cultured primary fibroblasts using mouse embryonic
219 fibroblasts (MEFs). MEFs were treated with CD63-FLAG tagged EVs or control CD63 EVs and immune-stained with

220 an anti-FLAG antibody and imaged by immunofluorescence (Figure 4K). We observed dose dependent EV uptake into
221 MEFs (Figure 4L). These findings showed that the activity of EVs administered to full thickness wounds can be
222 monitored by assessing cell proliferation as a molecular endpoint for the activity of pro-reparative EVs and that the
223 uptake of EVs can be localized using molecular tags such as the FLAG tag.

225 **Regulation of miRNA EV payloads isolated from diabetic obese donor model.**

226 Studies of miRNAs in EVs in diabetic wounds have established their translational relevance in wound healing.¹³
227 Therefore, we analyzed changes in miRNA payloads from WT and db/db mice in our model. We performed miRNA
228 sequencing (miRNAseq) on EVs purified from WT and db/db donors harvested from the PVA sponge model and
229 identified statistically significant changes in miRNAs from three biological replicates from WT and db/db EVs (Data has
230 been archived at NCBI #GSE242496) (Figure 5A). While many EV miRNAs were similar between WT and db/db EVs
231 (Figure 5B), consistent with the concept many miRNAs could be considered housekeeping miRNAs.^{57,58} However, of
232 the miRNAs that were down-regulated more than 2 fold in db/db vs. WT EVs, changes in the following miRNAs were
233 statistically significant: miR-425-5p (2.68 fold decrease), 361-3p (3.15 fold decrease), 3068-3p (3.15 fold decrease), and
234 186-5p (2.02 fold decrease). The only miRNA that was significantly up-regulated in EVs from db/db vs. WT donors
235 more than 2-fold was miR-409-5p (2.38-fold increase) (Figure 5C). KEGG pathway analysis (Figure 5D) of the overall
236 changes of these db/db-regulated miRNAs were associated with signaling pathways relevant in diabetic wound healing
237 and complications such as stem cell regulation and AGE-RAGE signaling in diabetic complications that are relevant in
238 impaired wound healing in a diabetic obese model.⁵⁹ To better understand the potential targets of individual miRNAs
239 identified, we analyzed potential targets using miRPathDB v2.0 and performed a literature search as summarized in Table
240 S2. With this approach, we identified miR-425-5p as the lead candidate as it had also been recently reported to mediate
241 endothelial survival relevant to EV action in a streptozocin-induced diabetic mouse model,⁶⁰ stimulate cell proliferation
242 relevant to the Ki-67 readouts of the wound healing model^{60,61} and that miR-425-5p was the only miRNA predicted from
243 miRPathDB to mediate dysregulation of insulin signaling^{62,63}; all highly relevant to the db/db model used here. GO Term
244 analysis also provided additional candidate targets for miR-425-5p action suggesting roles in regulating hypoxia
245 inducible factor, cyclin-dependent kinase and CD44 (Supplementary Figure S4). Therefore, to better understand the
246 relevance of a specific miRNA we focused on a relevant *in vitro* model. Since we observed that myeloid cell types

247 comprised the vast majority of cells in PVA sponges as identified by scRNAseq (Figure 1), and that the collection of EVs
248 from cultured primary macrophages yields biologically active EVs,⁸ we used M-CSF to differentiate cells isolated from
249 PVA sponge implants from WT vs. db/db mice from which EVs were then collected for further analysis (Figure 5E).
250 Equivalent numbers of EVs were released into the conditioned media from db/db and WT macrophages (Figure 5F).
251 These EVs were subjected to qRT-PCR to measure changes in the levels of miR-425-5p in EVs from db/db vs. WT
252 macrophages and identified a significant decrease in miR-425-5p levels (15-fold decrease, $p < 0.0051$) in db/db EVs
253 compared to WT mouse EVs (Figure 5G). These *in vitro* findings focused on EVs collected from cultured macrophages
254 were consistent with *in vivo* miRNAseq studies of PVA sponge-derived EVs where both showed a down-regulation of
255 miR-425-5p levels in db/db vs. WT EVs. Therefore, we next focused on identifying a biological activity of miR-425-
256 5p-loaded EVs in the db/db wound model.

258 **Functional activity of miR-425-5p-loaded EVs in diabetic wounds.**

259 Having shown that db/db EVs isolated from cultured macrophages have reduced levels of miR-425-5p compared
260 to WT EVs (Figure 5G), we tested the *in vivo* biological activity of miR-425-5p-loaded EVs on wound healing compared
261 to a negative control miRNA. We used cel-miR-67 as a negative control as it is derived from *C. elegans* and associated
262 with minimal effects on eukaryotic cell signaling.^{57,63,64} In addition several control studies using fluorescently labeled
263 miRNA controls were performed to optimize the concentrations for loading EVs with specific miRNAs and validating
264 by vFC that the surface profile of canonical tetraspanins CD9 and CD63 were unchanged by treatment with Exofect
265 reagent (Supplementary Figure S5). We focused on using WT EVs for miRNA loading since although WT EVs are
266 known to be pro-reparative, our goal was to identify a miRNA payload that would substantially improve upon the known
267 pro-reparative activity of WT EVs from naïve mice. Therefore, to determine whether treatment with miR-425-5p-loaded
268 EVs would stimulate a pro-reparative phenotype in a wound healing assay, we treated full thickness wounds in recipient
269 db/db mice, observed the wounds over 14 days and performed image analysis over 14 days (Figure 6A). We observed
270 that treatment with miR-425-5p-loaded EVs significantly accelerated wound closure on Day 7 compared to standard WT
271 EVs from naïve mice (no loading with any miRNA) (Figure 6B; $p < 0.005$), consistent with the hypothesis that pro-
272 reparative activity of WT EVs was increased by loading EVs with miR-425-5p. Additional controls comparing miR-
273 425-5p-loaded EVs with negative control miRNA, Mock-loaded EVs (i.e., treated with the Exofect reagent but lacking

274 miRNA), or saline alone demonstrated the pro-reparative activity of miR-425-5p-loaded EVs in wound healing on Days
275 7, 10 and 14 (Figure 6C; $p < 0.0001$). Based on our observation that treatment with WT EVs led to an increased number
276 of Ki67⁺ basal keratinocytes in wound healing (Figure 4), we analyzed the effect of miR-425-5p-loaded EVs on cell
277 proliferation in treated wounds as a molecular endpoint for the accelerated wound healing. We observed an increase in
278 Ki67⁺ basal keratinocytes (Figure 6D) that was quantified and statistically significant (5.2-fold increase, $p < 0.0024$)
279 compared to a negative control miRNA mimic-loaded EVs (Figure 6E). Analysis of H&E histology following treatment
280 with miR-425-5p-loaded EVs, negative control EVs, or saline controls further defined the effects of EV treatment (Figure
281 6F). Treatment with miR-425-5p-loaded EVs led to a statistically significant increase in the number of cells (Figure 6G,
282 based on blue box on margins of Figure 6F; 1.6-fold increase, $p < 0.0001$), but no significant changes in epidermal
283 thickness (Figure 6H, centered on the wound bed), or collagen staining based on a Masson's Trichrome stain (Figure 6I;
284 Image J analysis of blue staining). We did observe an overall increase in the differentiation of the underlying dermis that
285 was associated with increased vascularity based on H&E staining (Supplementary Figure S6A and B). However, the
286 density of CD31⁺ blood vessels per high powered field was similar between treatment with miR-425-5p-loaded EVs vs.
287 Neg-miR-loaded EVs (Supplementary Figure S6C and D). Therefore, the effects of treatment with miR-425-5p-loaded
288 EVs on blood vessels in this model may be indirect because it was associated with a robust pro-reparative phenotype or
289 may be direct by promoting endothelial survival as recently proposed.⁶⁰ Based on the translational relevance of our
290 studies of miR-loaded EVs on wound healing, we next determined whether loading of EVs with miRNA using Exofect
291 would lead to a significant amount of miRNA attached to the surface or would miRNAs be internalized and protected by
292 the lipid membrane. Therefore, we tested the effect of an *in vitro* nuclease treatment on isolated EVs using benzonase.⁶⁵
293 qRT-PCR was performed to measure changes in levels of miR-425-5p from vehicle vs. benzonase-treated EVs. We
294 observed no substantial differences, consistent with miRNAs being present within the EV and thus protected from
295 benzonase activity (Supplementary Figure S7).

296 Based on the pro-reparative effect miR-425-5p-loaded EVs on wound healing (Figure 6C) associated with the
297 increased proliferation of basal keratinocytes (Figure 6D and E), we focused on the identification of soluble mediators
298 such as cytokines and adipokines that could mediate signaling between cell layers in the skin. Therefore, we performed
299 a cytokine analysis testing a panel of 24 cytokines/adipokines to quantify relevant changes in inflammation mediators.⁶⁶
300 Whole cell lysates of wound tissue treated with miR-425-5p-loaded EVs were compared with tissues treated with

301 negative control miRNA-loaded EVs as described above. We observed significant increases in several factors, including
302 Adiponectin (2.4-fold increase, $p < 0.0009$), IL-1 α (2.3-fold increase, $p < 0.002$), and Serpin E1 (1.9-fold increase, $p <$
303 0.037), along with many other factors that were unchanged (Supplementary Figure S8). Based on the relevance of
304 Adiponectin as an important mediator of glucose metabolism in diabetic obese models,^{67,68} the uptake of FLAG-tagged
305 EVs into fibroblasts (Figure 4), and the general abundance of fibroblasts in the wound bed, we focused on testing whether
306 macrophage-derived EVs containing miR-425-5p (Figure 5G) could stimulate fibroblasts *in vitro*. Therefore, we
307 assessed whether treatment of MEFs with miR-425-5p-loaded EVs would stimulate Adiponectin expression *in vitro*
308 (Figure 6K), as predicted from *in vivo* treatments with miR-425-5p-loaded EVs stimulating Adiponectin expression
309 (Figure 6J). We subjected cultures of MEFs to 48 h treatment with miR-425-5p-loaded EVs compared to negative control
310 miRNA-loaded EVs as prepared for the *in vivo* studies above. We observed by immunoblotting of whole cell lysates
311 that miR-425-5p-loaded EVs led to a 1.4-fold increase in Adiponectin expression compared to treatment of MEFs with
312 control EVs (Figure 6L), using actin levels as a loading control. Although it remains unclear whether miR-425-5p has a
313 direct effect on the Adiponectin mRNA based on predicted binding sites of miR-425-5p, these findings suggest that
314 treatment of wounds *in vivo* or MEFs *in vitro* with miR-425-5p-loaded EVs leads to increases in Adiponectin expression.
315 In a model where macrophage-derived EVs promote intercellular signaling such as the release of EVs from macrophages
316 that stimulate fibroblasts, defining cell type-specific EV release with a genetic tool would provide important insights.

317 318 **Cell type-specific tracking of EV release and uptake.**

319 To address the question of cell type-specific EV release, we used a Cre-lox system for the regulated expression
320 of a fluorescent EV reporter, the tetraspanin CD9 as a fusion to GFP. Cell profiling of PVA sponge donor site using
321 scRNAseq showed high numbers of macrophages and related cell types (Figure 1), while immunohistochemistry of full
322 thickness wounds showed high numbers of F4/80⁺ macrophages distributed in the adipose layer (Supplementary Figure
323 S9). Therefore, we selected transgenic mice that expressed the Cre recombinase in macrophages for comparison with
324 transgenic mice expressing Cre in other skin-relevant cell types such as endothelium (TEK) and keratinocytes (KRT14).
325 Each tissue-specific transgenic Cre mouse line was crossed with mice expressing the CD9:GFP, termed the TIGER
326 reporter (Transgenic inducible GFP EV reporter; Figure 7A).²⁴ Tissue specific expression of CD9-GFP was under the
327 control of an upstream lox-STOP-lox cassette and crossed with transgenic mice expressing Cre under the control of the

328 LysM promoter (LysM-Cre) to assess the expression and release of GFP⁺ EVs from myeloid immune cells like
329 macrophages and monocytes. Crosses with TEK-Cre and CD9-GFP mice were performed in parallel with crosses with
330 TEK-Cre x CD9: GFP and KRT14-Cre x CD9-GFP. We first established the expression of GFP in each of the transgenic
331 mouse lines by analyzing cells recruited into the PVA sponge implants in parallel with the collection of donor EVs as
332 described above (Figure 7B). In addition, laser scanning confocal microscopy of PVA sponge implants was performed
333 for each genotype to establish positive controls for each of the mouse models (i.e., TEK-CD9-GFP, LysM-CD9-GFP and
334 KRT14-CD9-GFP; Supplementary Figure S10). For each donor genotype, cells (Figure 7B) and EVs (Figure 7C) were
335 purified from the PVA sponge implants as described above. Standard cell flow cytometry was performed for cells
336 collected where we observed that LysM-CD9-GFP and TEK-CD9-GFP mice expressed GFP. Since the surgical
337 placement of PVA sponge implants was between the adipose and dermal layers, few KRT14⁺ cells migrated or infiltrated
338 the PVA sponge implant in KRT14-CD9-GFP mice (Figure 7B and Supplementary Figure S10), although KRT14⁺
339 keratinocytes were present in intact overlying skin (data not shown). Analysis of EVs purified from PVA sponge implants
340 of each genotype focused on LysM-CD9-GFP mice that released high numbers of bright GFP⁺ EVs. In contrast, there
341 were few TEK-CD9-GFP⁺ or KRT14-CD9-GFP EVs (Figure 7C). We proceeded to further assess the distribution of
342 macrophage-derived EVs (i.e., LysM-CD9-GFP EVs) based on their abundance relative to other cell type-specific
343 promoters tested (Figure 7B) by treatment of full thickness wounds of db/db mice (Figure 7D). We observed that GFP⁺
344 EVs or accumulations of GFP⁺ EVs could be observed by confocal microscopy in wounds treated with LysM-CD9-GFP
345 EVs compared to the lack of signal in images of wounds treated with non-fluorescent controls EVs isolated from sibling-
346 matched controls lacking the Cre driver genes (Figure 7E). To determine whether LysM-CD9-GFP EVs could be
347 localized in fibroblasts based on a model of EV uptake by fibroblasts in the wound bed, we first established the
348 distribution of fibroblasts in the wound site by immunostaining full thickness wound sites with an anti-vimentin antibody
349 (Figure 7F). Imaging of both the left and right sides of the wound show the distribution of vimentin⁺ fibroblasts on the
350 wound margin (Figure 7F, sides of the images of the left and right panels) and the wound bed (Figure 7F, bottoms of the
351 images of the left and right panels). These low magnification images provide landmarks for the wound margins (i.e.,
352 sides of the wound) vs. the wound bed (i.e., bottom of the wound), and the negative control images for wounds treated
353 with WT non-fluorescent EVs (Figure 7F) vs. wounds treated with LysM-CD9-GFP EVs (Figure 7G). These
354 representative low magnification images (Figure 7F and G) were further analyzed at higher magnification to localize the

355 accumulation of LysM-CD9-GFP EVs in replicate high power fields of the wound margin (Figure 7H, based on red box
356 corresponding to Figure 7D), and in the wound bed (Figure 7I, based on blue boxes corresponding to Figure 7D). These
357 imaging studies established that populations of LysM-CD9-GFP EVs were co-localized with vimentin⁺ fibroblasts in the
358 wound margin (Figure 7H) and in the wound bed (Figure 7I). While these co-localization analyses did not exclude the
359 possibility of CD9-GFP uptake into other cell types, these studies provided insights into the distribution of EV uptake in
360 a complex microenvironment. Furthermore, EVs purified from a specific cell type such as macrophages express surface
361 proteins that may be relevant to their tropism and activity.

362 363 **DISCUSSION**

364 The healthy wound healing response is characterized by coordinated phases of hemostasis, inflammation,
365 proliferation, and remodeling, however, many aspects of the molecular and cellular basis of this response remain poorly
366 understood. The dysregulation of the coordinated response that is associated with impaired wound healing has led us to
367 identify defects in intercellular signaling between cell layers in the skin with a focus on EVs and their payloads as
368 mediators of these processes. We propose that macrophage-derived EVs from resident macrophages have biologically
369 active payloads that are internalized by skin fibroblasts to stimulate signaling, and specific adipokine expression that
370 leads to a pro-reparative response that includes proliferation of overlying keratinocytes.

371 The composition and function of EVs released into biological fluids and cultured media, which are heterogenous
372 in origin, is dependent on the cells that produce them. There are few *in vivo* models that have mapped the landscape of
373 cells and EVs in a well-defined microenvironment with genetic tools. Here, we focused on wound healing in db/db mice
374 as a genetic model of impaired wound healing to show that EVs enriched from db/db donors have impaired wound
375 healing activity and reduced capacity to signal specific molecular endpoints in fibroblasts that was associated with
376 stimulating proliferation of basal layer epithelial cells. miRNAseq of EVs isolated from db/db vs. WT mouse donors
377 revealed a reduction in the miR-425-5p. miR-425-5p, especially when loaded into EVs, has been associated with
378 dysregulated insulin signaling in some models⁶¹ or as a pro-survival endothelial factor in db/db EVs in other models.⁶⁰
379 We show that miR-425-5p was differentially expressed in macrophage-derived EVs isolated from db/db vs. WT mice,
380 that wounds treated with miR-425-5p-loaded EVs promoted wound closure, and identified a miR-425-5p-mediated
381 upregulation of Adiponectin in the wound bed *in vivo* and in cultured fibroblasts *in vitro*. Based on our findings that

382 macrophage-derived EVs signal to other cell types in the wound, we used a cell type-specific CD9-GFP reporter model
383 to define the distribution and map uptake of macrophage-derived EVs into fibroblasts. Together, these studies defined a
384 population of macrophage-derived EVs that are internalized by dermal fibroblasts to regulate Adiponectin expression
385 associated with promoting wound healing and cell proliferation.

386 Recent work from our lab has focused on the identification of quantitative changes in protein payloads in EVs
387 isolated from db/db vs. WT donor mouse models with a goal of engineering EVs to deliver these pro-reparative payloads
388 to the wound bed. For example, we identified a down-regulation of proteins associated with extracellular matrix
389 remodeling and innate immunity⁸ and re-expressed select serine protease inhibitors to reverse the impaired wound
390 healing phenotype of db/db recipients. Here we focused on miRNA analysis of db/db vs. WT EV payloads and identified
391 several miRNAs that were down-regulated in db/db EVs and others that were up-regulated. To establish the function of
392 a specific miRNA as an example of how to validate the activity of candidate miRNA, we selected miR-425-5p for testing,
393 along with negative controls for activity, and positive controls for EV loading. While several miRNA profiling studies
394 have identified miRNAs that are relevant in impaired wound healing, comparatively fewer have assessed the activity of
395 specific EV-loaded miRNAs in wound healing.⁶⁹ Therefore, we used a combination of target pathway analysis databases
396 and literature review to prioritize specific miRNAs for functional testing. While our studies were limited to the
397 identification of miRNAs dysregulated in the db/db PVA sponge model, further studies with antagomirs, miRNA
398 knockout mice and miRNA activity reporter tools will be important to better understand loss of function phenotypes for
399 specific miRNAs.⁷⁰⁻⁷³ One of the limitations of functional testing of endogenous miRNA-loaded EVs in the field is the
400 poorly understood nature of miRNA abundance and distribution in a population of EVs.^{74,75} For our analysis of miRNA
401 activity, we focused on testing a miRNA that was down-regulated in db/db EVs that could then be delivered in an EV to
402 restore a pathway(s) in a wound bed treated with EVs loaded with that down-regulated miRNA. To this end we identified
403 miR-425-5p as one of the most relevant miRNAs based on the obese hyperglycemic phenotype of the db/db mice from
404 which EVs were collected and analyzed by miRNAseq, and reports that linked miR-425-5p action to the regulation of
405 insulin responsiveness.^{62,63} We suggest that miR-425-5p regulated insulin signaling may be linked to the miR-425-5p-
406 mediated changes in the expression of an adipokine like Adiponectin in the regulation glucose sensitivity.⁷⁶ We proposed
407 that miR-425-5p-loaded EVs may have a role in stimulating secreted factors in adjacent cell types that promote wound
408 healing. In addition to Adiponectin, future studies may focus on other candidates such as IL-1 α and Serpin E1, also

known as plasminogen activating inhibitor, that are relevant in inflammation and angiogenesis, respectively. Therefore, with recent studies identifying an activity for miR-425-5p in endothelial cells as a pro-survival regulator of endothelial cells that promotes wound healing in a streptozocin model of impaired diabetic wound healing⁶⁰ we examined the effects of miR-425-5p-loaded EVs in a genetic db/db model. Although we did not observe a significant difference in CD31⁺ blood vessel density, systematic approaches that test miRNA action in complex tissues will be necessary to better define cell type-specific effects of miRNAs.

With a significant interest of the EV field focused on how to define EV source and uptake, we focused on an *in vivo* model where the EV source is defined by cell types relevant to cutaneous wound healing, like macrophages. We show that macrophage-derived EVs can be tracked and purified for adoptive transfer studies using cell type-specific promoters to follow GFP fluorescence by flow cytometry and microscopy. Fluorescent reporter systems utilizing CD9-GFP fusions,²⁴ as we have done for cutaneous injury models, along with recent studies using fusion reporters with CD81 for EV tracking from blood, brain, liver and ovary,²⁶ provide important insights into the relevant cell types and biodistribution *in vivo*. The development of pH-dependent fluorescent EV reporters that distinguish between EVs in acidic late endosomal MVBs vs. the release of EVs in neutral extracellular space and for tracking EV uptake provide further support for the utility of tetraspanin:fluorescent reporters in the understanding of EV release and uptake.⁷⁷ These tetraspanin:fluorescent reporters are important tools to understand the biodistribution and activity of nucleic acid payloads like functional miRNAs and guide RNAs that direct CRISPR/Cas9 machinery for gene editing target cells.⁷⁸ We have also shown here that direct tagging of tetraspanins, like the FLAG tagging of CD63 on EVs takes advantage of a well-established molecular tool that also has utility in purification strategies.⁷⁹

The overall novelty of our studies is that we establish an *in vivo* system for the efficient and high yield purification of EVs that can be applied to various animal models to define the biological activity and assess molecular endpoints of engineered EVs. These engineered EVs can deliver pro-reparative payloads identified by -omic approaches that are most relevant in accelerating the resolution of inflammation and promoting the proliferation of specific cell types relevant in tissue repair. With the application of fluorescent, genetic and other advanced EV tracking technologies, lineage mapping of the source of EV release and uptake of EVs into recipient cells can lead to a molecular understanding of intercellular signaling mediated by EVs between skin layers in wound healing.

435

436 **MATERIALS AND METHODS**437 **Mouse model for EV collection from PVA sponges**

438 All mouse studies were conducted in accordance with the Institutional Animal Care and Use Committee of the
439 University of California San Diego. 12-16 week old WT and db/db mice (B6.BKS(D)-Lepr^{db/db}/J; The Jackson
440 Laboratory #000697, Bar Harbor, Maine) where db/db mice had a blood glucose level > 300 mg/dL and body weight
441 >45 g, criteria for the diabetic obese model^{80,81}. Mice were prepared for the subcutaneous implantation of three Polyvinyl
442 Alcohol (PVA) sponges (Cat# SQ5000, PVA Unlimited Inc., Warsaw, IN) by shaving and topical treatment with
443 depilatory cream of dorsal skin. Following PVA sponge implantation, skin was closed with nylon monofilament sutures
444 and incubated for 7 days. PVA sponges were then harvested by direct transfer of all three sponges into 1 mL of phosphate-
445 buffered saline for the recovery of cells infiltrating the sponges and associated fluid flushed from the sponges that
446 contained EVs. Centrifugation at 3,000 × g for 5 min separated cells into a pellet that was used for scRNAseq, while the
447 supernatant of the PVA sponge fluid contained EVs for further analysis.

448 For the goal of identifying cell type-specific sources of EVs, we used transgenic mice expressing a CD9-TurboGFP
449 reporter targeted to extracellular vesicles under the control of a lox-STOP-lox cassette to facilitate cell type specific
450 expression based on promoters driving the expression of Cre in specific cell types, termed TIGER knock-in mice.²⁴ The
451 following three crosses were performed with these CD9-GFP mice (B6;129S1-Gt(ROSA)26Sor^{tm1(CAG-CD9/GFP)Dmfl}/J;
452 Jackson Laboratories #033361). For expression of the CD9-GFP reporter in macrophages/monocytes mice were crossed
453 with a LysM-Cre mice (B6.129P2-Lyz2^{tm1(cre)lfo}/J; Jackson Laboratories #004781). For the expression of the CD9-GFP
454 reporter in endothelial cells, mice were crossed with TEK-Cre mice (B6.Cg-Tg(TEK-cre)12Flv/J; Jackson Laboratories
455 #004128). For the expression of CD9-GFP reporter in keratinocytes, mice were crossed with KRT14-Cre mice (B6N.Cg-
456 Tg(KRT14-cre)1Amc/J; Jackson Laboratories #018964) (Table S2).

457

458 **scRNAseq**

459 scRNAseq was performed on cells recovered from PVA sponges implanted into each of 3 different WT mice that
460 were then pooled and compared with similarly pooled cells from each of 3 different db/db mice. scRNAseq data was

461 archived at NCBI (GSE242497). In brief, 1×10^5 cells were collected from the PVA sponges from each mouse, pooled
462 and then 1×10^4 cells were loaded on the 10x Chromium Next GEM using the Single Cell 3' Reagent (v3.1) with gel
463 beads and master mix for cell capture and GEM generation (Cat # 1000147, 10X Genomics, San Francisco, CA).
464 Subsequently, samples underwent GEM reverse transcription cleanup, cDNA amplification, and 3' gene expression
465 library construction according to the manufacturer's instructions (10x Genomics). Constructed libraries were then
466 sequenced on HiSeq sequencers (Illumina, San Diego, CA) using paired end reads at the University of California, San
467 Diego Institute for Genomic Medicine (IGM) (Table S3 and S7). scRNAseq data was demultiplexed, giving rise to 2
468 FASTQ files per sample (4 FASTQ files in total), and aligned to the reference murine genome GRCm38 (mm10, v2020-
469 A) into single cells using the Cell Ranger Count pipeline (10x Genomics, v7.0.0) with the following settings for each
470 sample, independently— Library Type: Single Cell 3' Gene Expression; check library compatibility: true; chemistry:
471 auto; include introns: true; no_bam: false; no secondary analysis: false. Cell Ranger Count outputs for each sample were
472 then aggregated and normalized into a single gene expression matrix using the Cell Ranger Aggr pipeline (10x Genomics,
473 v7.0.0) with the follow settings— no secondary analysis: false; normalization mode: mapped. Running Cell Ranger Aggr
474 yielded approximately 18,000 post-normalizations mean reads per cell. Further data filtering and analysis were conducted
475 using Loupe Browser (10x Genomics, v6.1.0). Quality control included omitting cells with >15% Mitochondrial UMIs
476 per barcode (Linear) or <9.185 Genes per Barcode (Log2); cells that passed these quality control filters were included in
477 downstream analysis. The top 10 principal components were used for graph-based clustering, and the following settings
478 were applied for dimensionality reduction via uniform manifold approximation and projection (UMAP) analysis—
479 Minimum Distance: 0.1; Number of Neighbors: 15.

481 EV isolation and analysis

482 EV studies addressed the methodological recommendations of the Minimal Information for Studies of
483 Extracellular Vesicles 2018 (MISEV 2018)⁸² including nomenclature, collection/pre-processing, EV
484 separation/concentration, EV characterization, functional studies, and reporting that are all archived at EV-TRACK
485 (evtrack.org; #EV230979). For the isolation of EVs from PVA sponge implants, the cell-free supernatant was subjected
486 to two $10,000 \times g$ spins for 30 min at 4° C followed by size exclusion chromatography (SEC) (Cat # ICI-70, IZON,

487 Medford, MA) and collection of 22 fractions of 700 μ L each. EVs from cultured cell media were enriched using
488 Exoquick reagent (Cat # EQUltra-20A-1, System Biosciences, Palo Alto, CA) following the manufacturer's protocol.

490 **Single vesicle flow cytometry (vFC)**

491 EV concentration, size, and analysis of surface proteins and fluorescent proteins were measured by single
492 vesicle flow cytometry (vFC) using a commercial assay based on a fluorescent lipophilic membrane dye, vFRed (vFC
493 Assay kit, Cat # CBS4HP-1PE, Cellarcus Biosciences, San Diego, CA), using a CytoFLEX flow cytometer (Model S,
494 V4-B2-Y4-R3, Beckman Coulter, Indianapolis, IN) (Table S7). The flow cytometer was calibrated for vesicle size and
495 immunofluorescence (IF) using fluorescent intensity standard beads (nanoRainbow, Cellarcus) and antibody capture
496 beads (nanoCal, Cellarcus),⁸³⁻⁸⁵ and showed a size (diameter) limit of detection (LOD) of ~80 nm and an IF LOD of ~25
497 PE MESF. Samples were diluted (optimal dilution determined in preliminary experiments), stained with vFRed and PE-
498 conjugated antibodies (See Table S5 and S6), subjected to a 1000-fold post-stain dilution, and 100 μ L measured on the
499 flow cytometer at a flow rate of 60 μ L/min. Data were analyzed using FCS Express (Dotmatics/Denovo Software) and a
500 standardized layout used to apply gating, compensation, and calibration (Cellarcus). Single vesicle flow cytometry data
501 was archived at flowcytometry.org (ID: FR-FCM-Z749) with a MIFlowCyt Score of 95%.

502 **EV characterizations by immunoblotting, electron microscopy, and multiplex analysis**

503 Lysates of EVs isolated from PVA sponges, paired along with whole cell lysates (WCLs) from the sponge
504 implants, were prepared in RIPA lysis buffer. Loading of WCLs were normalized by protein quantification with a BCA
505 assay (Cat# 23225, ThermoFisher, Carlsbad, CA) while loading of EVs was normalized to EV counts based on vFC
506 analysis as described above. Nonfat Dry Milk (Cell Signaling Technology, Denver, MA) was used for blocking in Tris-
507 buffered saline with 0.05% Tween 20 and primary antibodies incubated overnight at 4 °C. Table S4 details primary and
508 secondary antibodies used for immunoblotting. Immunoblots were detected with horseradish peroxidase-conjugated
509 secondary, incubated with enhanced chemiluminescent reagent (Cat# 32209, ThermoFisher) and detected with an IVIS-
510 Lumina Imager (Perkin Elmer). For imaging of EVs by transmission electronic microscopy, EV samples were applied
511 onto EM grids, washed, and stained with uranyl acetate and images obtained with a Jeol 1400 plus transmission electron
512 microscope at 80 KeV. For the multiplex analysis of EVs present on EVs, a bead-based screen for 37 EV surface proteins

513 was used (MACSPlex Exosome Kit, Cat#130-122-211, Miltenyi-Biotec, San Diego, CA), and followed manufacturer's
514 recommendations. Data was analyzed with data analysis template using MACSQuant (ver. 2.12.2) (Miltenyi-Biotec).

516 **EVs studies to assess wound healing, signaling and uptake *in vivo*.**

517 To assess the activity of EVs upon the kinetics of wound closure, EVs were purified from PVA sponge implants
518 as described above and used to treat full thickness splinted 4 mm wounds as previously described.^{86,87} Briefly, a silicone
519 ring (Cat# GBLRD476687, Grace Bio-labs, Bend, OR) was immobilized with 4-0 nylon sutures (Cat # 50-118-0628,
520 ThermoFisher) around each wound and immediately treated with $5-7 \times 10^6$ EVs in a volume of 50 μ l of PBS per wound
521 and covered with 3M Tegaderm (Cat #, 264435, Mckesson, Irving, TX).⁸⁶ Wounds were imaged with a Galaxy S10e
522 (1200 pixels, AF, F1.5/F2.4 super speed dual pixel, Samsung) and analyzed by Image J (1.53e version). Tissues were
523 harvested for histology analysis by fixation of skin wound samples in paraformaldehyde into paraffin at the UCSD Tissue
524 Technology Shared Resource (TTSR) that prepared slides stained with Hematoxylin/Eosin and Masson's Trichrome
525 stains, to detect collagen staining in blue. Immunohistochemical staining to localize Ki-67 (1:50; Cat #,16667, Genetex,
526 Irvine, CA) immunohistochemical staining was performed with a Intellipath Automated IHC Stainer (Biocare, Pacheco,
527 CA) by the TTSR, while immunostaining with anti-FLAG antibody (1:100; Cat # 14793, Cell Signaling Technologies)
528 and anti-F4/80 (1:100, Cat# 70076, Cell Signaling Technologies) was performed with HRP detection SignalBoost
529 reagents (Cat# 8114 and 8059, Cell Signaling Technologies). Tissues harvest for analysis for cytokines/adipokines was
530 performed with a Proteome Profiler (Cat # ARY028, R&D Systems, Minneapolis, MN) and followed manufacturers
531 recommendations for detection and quantification with an IVIS-Lumina imaging system. Analysis of wounds treated
532 with CD9-GFP⁺ EVs was performed by cryosectioning treated wounds with a cryostat (Model CM1850, Leica,
533 Davisburg, MI), imaged with a Nikon Confocal microscope (Model AXR, Tokyo, Japan). Counterstaining of CD9-GFP⁺
534 EVs was performed with an anti-vimentin antibody (1:200, Cat # 5741, Cell Signaling Technologies) to localize
535 fibroblasts and detected with an Alexa 546 secondary antibody (1:1,000, Cat #A11010, ThermoFisher). All H&E,
536 Masson's Trichrome and immunofluorescence images were analyzed with Image J software.

538 Generation and testing of FLAG-tagged EVs

539 An epitope tagged variant of CD63 was created by cloning the FLAG sequence (DYKDDDDK) at amino acid 1397
540 on the second extracellular loop of CD63. Following transient transfection of HEK293T cells (Cat # CRL-1573, ATCC,
541 Manassas, VA) with Lipofectamine 3000 (ThermoFisher) per manufacturer's directions, the expression on the cell
542 surface was validated by immunoblot with an anti-FLAG antibody (Cat# F-1804, Sigma, St. Louis, MO). vFC was
543 performed to detect expression of FLAG-tagged CD63 on EVs isolated from the conditioned media of transfected cells
544 using a PE-conjugated anti-FLAG antibody (Cat# CBS18-PE-100T, Cellarcus Biosciences, San Diego, CA). Uptake of
545 FLAG-tagged EVs into primary MEFs was assessed by treatment of $1e^6$ cultured primary MEFs (Cat# SCRC-1008,
546 ATCC) with 2×10^9 EVs in a volume of 100 μ l, incubated for 48 h, fixed, and stained with an anti-FLAG tag antibody
547 (1:100, Cat#14793, Cell Signaling Technologies) and a fluorescent anti-Rabbit Alex Fluor 488 (Cat# A-11008,
548 ThermoFisher).

550 *In vitro* analysis of macrophage-derived EV miRNAs and Adiponectin expression

551 Primary macrophages prepared from PVA sponges were cultured for the collection of macrophage-derived EVs
552 to measure levels of miR-425-5p. Briefly, PVA sponges were implanted into mice, incubated for 7 days and cells
553 harvested as described above. Cells were cultured in RPMI media supplemented with 10% fetal bovine serum and 25
554 ng/ml M-CSF (Cat # 14-8983-80, Life Technologies, Carlsbad, CA) for 7 days, with a media change at 3 days. Flow
555 cytometry was performed on cells incubated for 7 days in M-CSF with an anti-F4/80 antibody, which was used to verify
556 $>90\%$ F4/80⁺ cells. After the 7 day incubation, cells were transferred to RPMI media supplemented with 10% exosome-
557 depleted FBS (SBI) and conditioned media collected after an additional 7 day incubation. From this conditioned media,
558 EVs were harvested using Exoquick per manufacturer's recommendation, and EVs analyzed for qPCR for miR-425-5p
559 as described below. The activity of miR-425-5p-loaded EVs upon the stimulation of MEFs was determined by incubation
560 of EVs for 48 h, then measured by immunoblotting for adiponectin with an anti-adiponectin antibody (Cat #MA1-054,
561 ThermoFisher) and followed by detection with an IVIS-Lumina Imaging system.

562 miRNA sequencing, analysis, EV loading and RT-PCR

563 For the analysis of miRNA EV payloads, EVs were purified by SEC from 7 day PVA sponge implants of WT
564 vs. db/db mice. To obtain a more concentrated sample for RNA extraction, purified EVs were subjected to
565 ultracentrifugation (259,000 x g, for 70 minutes, Beckman Optima, Rotor TLA 120.2, k-factor 8), the supernatant
566 discarded, and the pellet extracted to obtain RNA using Trizol (ThermoFisher). RNA quality and quantity were analyzed
567 with a Bioanalyzer 2100 (Agilent, CA, USA), and 1 µg of RNA used to prepare a small RNA library using a TruSeq
568 Small RNA Sample Prep Kit (Illumina, San Diego, CA). Single-end 50 bp sequencing was performed on an Illumina
569 HiSeq 4000 (LC Sciences, Houston, TX) with initial processing of raw reads using proprietary software ACGT101-miR
570 (LC Sciences) to remove adapter dimers, foreign sequences, low-complexity fragments, common RNA families (e.g.
571 rRNA, tRNA, snRNA, snoRNA) and repetitive sequences. Sequences were mapped against species-specific miRNA
572 precursor sequences available in miRBase 21.0 using NCBI BLAST to identify known and potentially novel miRNAs,
573 with the alignment process allowing for length variation at both the 3' and 5' ends of the sequence and a tolerance for
574 one mismatch within the sequence. Identification of known miRNAs involved recognition of unique sequences aligned
575 with the mature miRNAs of a specific species located on the hairpin arm. At the same time, sequences aligning with the
576 opposite arm of a known species-specific precursor hairpin without an annotated mature miRNA were classified as
577 candidates for new 5p- or 3p-derived miRNAs. Unmapped sequences were aligned against the precursor sequences of
578 selected species (excluding certain species) within miRBase 21.0 and subjected to further analysis. These mapped pre-
579 miRNAs were then cross-referenced with the genome of a specific species to confirm their genomic location and
580 classified as known miRNAs. The remaining unmapped sequences were subjected to BLAST searches against the
581 genomes of specific species. Hairpin RNA structures containing these sequences were predicted using RNA fold software
582 (<http://rna.tbi.univie.ac.at/cgi-bin/RNAWebSuite/RNAfold.cgi>) using the 80 nucleotides flanking the sequence.⁸⁸⁻⁹⁰ For
583 the analysis of differentially expressed miRNAs, a normalization based on deep-sequencing counts. To predict the genes
584 targeted by most abundant miRNAs, two computational target prediction algorithms (TargetScan 50 and Miranda 3.3a)
585 were used to identify miRNA binding sites. Finally, the data predicted by both algorithms were combined and the
586 overlaps were calculated. The GO terms and KEGG Pathway of these most abundant miRNAs, miRNA targets were also
587 annotated. For loading miRNAs into EVs isolated from WT PVA sponge donors, 100 µL of EVs at a concentration of 6
588 x 10⁶ PVA EVs/µL were mixed with 200 pmoles of miR-425-5p (Cat# C-310988-01-0050, Horizon, San Diego, CA) or
589 a negative control cel-miR-67 (Cat# CN-001000-01-50, Horizon) in a volume of 200 µL following manufacturer's

590 recommendations for Exofect kit (Cat# EXFT20A-1, System Biosciences, SBI, Palo Alto, CA). Conditions for EV
591 loading with miRNAs were optimized with a Cy3-labeled miR control (SBI). miR-loaded EVs and followed
592 manufacturer's recommendations for purification. qRT-PCR was performed on CFX96 (Bio-Rad) using the TaqMan™
593 Fast Advanced Master Mix for qPCR (Cat# 4444556, ThermoFisher) and TaqMan™ Advanced miRNA Assay
594 (mmu481161_mir) (Cat# A25576, ThermoFisher). To confirm the expression of miR-425-5p in EVs collected from M-
595 CSF-differentiated PVA macrophages, we extracted RNA using a mirVana™ miRNA Isolation Kit (Cat#AM1560,
596 ThermoFisher, Carlsbad, CA) following manufacturer's protocol. cDNA was synthesized for each sample using the
597 TaqMan™ Advanced miRNA cDNA Synthesis Kit (Cat# A28007, ThermoFisher). and qPCR performed with a
598 TaqMan™ Fast Advanced Master Mix (Cat# 4444556, ThermoFisher) and the TaqMan™ Advanced miRNA Assay
599 specific for mouse miR-425-5p (mmu481161_mir; '3-AAUGACACGAUCACUCCCGUUGA-5') (Cat# A25576,
600 ThermoFisher).

602 **Statistical analysis**

603 All statistical analyses were performed with Prism 6.0 (Graphpad Software). Data were expressed as the mean
604 \pm standard deviation (SD). Differences between different groups were compared by Student t-test (i.e., vFC) and two-
605 way ANOVA with multiple comparisons (i.e, wound healing assays), with statistically significant p-values indicated as
606 ****<0.0001, ***<0.001, **<0.005, *<0.05. All statistical analyzes and representative images presented and observed
607 in at least 3 independent experiments.

Detailed Reagent Supporting Information

Additional details on reagents, mice, software, kits, antibodies, and software are provided in Supplementary Tables S3-8.

DATA AVAILABILITY STATEMENT

scRNAseq (#GSE242496) and miRNAseq data (#GSE242497) produced in this study are accessible via GEO archives maintained by the NCBI. Vesicle flow cytometry data is deposited into flowrepository.org (#FR-FCM-Z749).

ACKNOWLEDGMENTS

Ann-Marie Hageny, Emelie Amburn, Katie Pool, and Michelle Bagood provided expert technical support. The UCSD Tissue Technology Shared Resources (TTSR) core at the Moores Cancer Center provided histology services, the UCSD Nikon Imaging Center confocal microscopy imaging services, and the UCSD Institute for Genomic Medicine for scRNA sequencing that utilized an Illumina NovaSeq 6000 purchased with funding from a National Institutes of Health SIF grant (#S10 OD026929). Schematics and the graphical abstract were created in Biorender.com under license agreement. This work was supported by National Institutes of Health grants (1 R01 GM140137 and 1 R35 GM149245) (BPE) and KL2TR001444 of CTSA funding through the UCSD CTRI (R.D.).

AUTHOR CONTRIBUTIONS

Conceptualization, D.J.P. and B.P.E.; Methodology, D.J.P., W.C., K.H., J.K., J.N.; Software D.J.P., W.C., S.S.; Validation, D.J.P., W.C.; Investigation, D.J.P., W.C., S.S., K.H., J.K., J.R., P.M., T.C., R.D., J.N., B.P.E; Resources, D.J.P., S.S., Data Curation, D.J.P., S.S.; Reagents, J.R. and P.M.; Writing-Original Draft, D.J.P., B.P.E.; Visualization, D.J.P., S.S., B.P.E.; Funding Acquisition B.P.E., P.M. and T.C.

DECLARATION OF INTERESTS

The laboratory receives funding support for EV tropism screening research that is unrelated to the studies described herein from Ionis Pharmaceuticals (B.P.E., P.M., and J.P.N.). J.P.N. is CEO of Cellarcus Biosciences.

KEYWORDS

Extracellular vesicles; Diabetic wound closure; miR-425-5p; single cell RNA sequence; macrophage; Adiponectin

641 **References**

- 642
- 643 1. Koh, T.J., and DiPietro, L.A. (2011). Inflammation and wound healing: the role of the macrophage. *Expert Rev*
- 644 *Mol Med* 13, e23. 10.1017/S1462399411001943.
- 645 2. Minutti, C.M., Knipper, J.A., Allen, J.E., and Zaiss, D.M. (2017). Tissue-specific contribution of macrophages
- 646 to wound healing. *Semin Cell Dev Biol* 61, 3-11. 10.1016/j.semcdb.2016.08.006.
- 647 3. Novak, M.L., and Koh, T.J. (2013). Phenotypic transitions of macrophages orchestrate tissue repair. *Am J*
- 648 *Pathol* 183, 1352-1363. 10.1016/j.ajpath.2013.06.034.
- 649 4. Larouche, J., Sheoran, S., Maruyama, K., and Martino, M.M. (2018). Immune Regulation of Skin Wound
- 650 Healing: Mechanisms and Novel Therapeutic Targets. *Adv Wound Care (New Rochelle)* 7, 209-231.
- 651 10.1089/wound.2017.0761.
- 652 5. Hoshino, A., Costa-Silva, B., Shen, T.L., Rodrigues, G., Hashimoto, A., Tesic Mark, M., Molina, H., Kohsaka,
- 653 S., Di Giannatale, A., Ceder, S., et al. (2015). Tumour exosome integrins determine organotropic metastasis.
- 654 *Nature* 527, 329-335. 10.1038/nature15756.
- 655 6. Pluchino, S., and Smith, J.A. (2019). Explicating Exosomes: Reclassifying the Rising Stars of Intercellular
- 656 Communication. *Cell* 177, 225-227. 10.1016/j.cell.2019.03.020.
- 657 7. Jeppesen, D.K., Fenix, A.M., Franklin, J.L., Higginbotham, J.N., Zhang, Q., Zimmerman, L.J., Liebler, D.C.,
- 658 Ping, J., Liu, Q., Evans, R., et al. (2019). Reassessment of Exosome Composition. *Cell* 177, 428-445 e418.
- 659 10.1016/j.cell.2019.02.029.
- 660 8. Park, D.J., Duggan, E., Ho, K., Dorschner, R.A., Dobke, M., Nolan, J.P., and Eliceiri, B.P. (2022). Serpin-
- 661 loaded extracellular vesicles promote tissue repair in a mouse model of impaired wound healing. *J*
- 662 *Nanobiotechnology* 20, 474. 10.1186/s12951-022-01656-7.
- 663 9. Qin, S., Dorschner, R.A., Masini, I., Lavoie-Gagne, O., Stahl, P.D., Costantini, T.W., Baird, A., and Eliceiri,
- 664 B.P. (2019). TBC1D3 regulates the payload and biological activity of extracellular vesicles that mediate tissue
- 665 repair. *FASEB J* 33, 6129-6139. 10.1096/fj.201802388R.
- 666 10. Qian, J., Park, D.J., Perrott, S., Patel, P., and Eliceiri, B.P. (2021). Genetic Background and Kinetics Define
- 667 Wound Bed Extracellular Vesicles in a Mouse Model of Cutaneous Injury. *Int J Mol Sci* 22.
- 668 10.3390/ijms22073551.
- 669 11. Silva, A.M., Teixeira, J.H., Almeida, M.I., Goncalves, R.M., Barbosa, M.A., and Santos, S.G. (2017).
- 670 Extracellular Vesicles: Immunomodulatory messengers in the context of tissue repair/regeneration. *Eur J*
- 671 *Pharm Sci* 98, 86-95. 10.1016/j.ejps.2016.09.017.
- 672 12. Veerman, R.E., Teeuwen, L., Czarnewski, P., Gucluler Akpınar, G., Sandberg, A., Cao, X., Pernemalm, M.,
- 673 Orre, L.M., Gabrielsson, S., and Eldh, M. (2021). Molecular evaluation of five different isolation methods for
- 674 extracellular vesicles reveals different clinical applicability and subcellular origin. *J Extracell Vesicles* 10,
- 675 e12128. 10.1002/jev2.12128.

- 676 13. Prasai, A., Jay, J.W., Jupiter, D., Wolf, S.E., and El Ayadi, A. (2022). Role of Exosomes in Dermal Wound
677 Healing: A Systematic Review. *J Invest Dermatol* *142*, 662-678 e668. 10.1016/j.jid.2021.07.167.
- 678 14. Sarcinella, A., Femmino, S., and Brizzi, M.F. (2023). Extracellular Vesicles: Emergent and Multiple Sources in
679 Wound Healing Treatment. *Int J Mol Sci* *24*. 10.3390/ijms242115709.
- 680 15. Pitt, J.M., Kroemer, G., and Zitvogel, L. (2016). Extracellular vesicles: masters of intercellular communication
681 and potential clinical interventions. *J Clin Invest* *126*, 1139-1143. 10.1172/JCI87316.
- 682 16. Deskins, D.L., Ardestani, S., and Young, P.P. (2012). The polyvinyl alcohol sponge model implantation. *J Vis*
683 *Exp.* 10.3791/3885.
- 684 17. Baird, A., Deng, C., Eliceiri, M.H., Haghi, F., Dang, X., Coimbra, R., Costantini, T.W., Torbett, B.E., and
685 Eliceiri, B.P. (2016). Mice engrafted with human hematopoietic stem cells support a human myeloid cell
686 inflammatory response in vivo. *Wound Repair Regen* *24*, 1004-1014. 10.1111/wrr.12471.
- 687 18. Crane, M.J., Daley, J.M., van Houtte, O., Brancato, S.K., Henry, W.L., Jr., and Albina, J.E. (2014). The
688 monocyte to macrophage transition in the murine sterile wound. *PLoS One* *9*, e86660.
689 10.1371/journal.pone.0086660.
- 690 19. Michaels, J.t., Churgin, S.S., Blechman, K.M., Greives, M.R., Aarabi, S., Galiano, R.D., and Gurtner, G.C.
691 (2007). db/db mice exhibit severe wound-healing impairments compared with other murine diabetic strains in
692 a silicone-splinted excisional wound model. *Wound Repair Regen* *15*, 665-670. 10.1111/j.1524-
693 475X.2007.00273.x.
- 694 20. Zhao, G., Hochwalt, P.C., Usui, M.L., Underwood, R.A., Singh, P.K., James, G.A., Stewart, P.S., Fleckman, P.,
695 and Olerud, J.E. (2010). Delayed wound healing in diabetic (db/db) mice with *Pseudomonas aeruginosa*
696 biofilm challenge: a model for the study of chronic wounds. *Wound Repair Regen* *18*, 467-477.
697 10.1111/j.1524-475X.2010.00608.x.
- 698 21. Park, S.A., Teixeira, L.B., Raghunathan, V.K., Covert, J., Dubielzig, R.R., Isseroff, R.R., Schurr, M., Abbott,
699 N.L., McAnulty, J., and Murphy, C.J. (2014). Full-thickness splinted skin wound healing models in db/db and
700 heterozygous mice: implications for wound healing impairment. *Wound Repair Regen* *22*, 368-380.
701 10.1111/wrr.12172.
- 702 22. Dhall, S., Do, D., Garcia, M., Wijesinghe, D.S., Brandon, A., Kim, J., Sanchez, A., Lyubovitsky, J., Gallagher,
703 S., Nothnagel, E.A., et al. (2014). A novel model of chronic wounds: importance of redox imbalance and
704 biofilm-forming bacteria for establishment of chronicity. *PLoS One* *9*, e109848.
705 10.1371/journal.pone.0109848.
- 706 23. McCann, J.V., Bischoff, S.R., Zhang, Y., Cowley, D.O., Sanchez-Gonzalez, V., Daaboul, G.D., and Dudley,
707 A.C. (2020). Reporter mice for isolating and auditing cell type-specific extracellular vesicles in vivo. *Genesis*
708 *58*, e23369. 10.1002/dvg.23369.
- 709 24. Neckles, V.N., Morton, M.C., Holmberg, J.C., Sokolov, A.M., Nottoli, T., Liu, D., and Feliciano, D.M. (2019).
710 A transgenic inducible GFP extracellular-vesicle reporter (TIGER) mouse illuminates neonatal cortical

- 711 astrocytes as a source of immunomodulatory extracellular vesicles. *Sci Rep* 9, 3094. 10.1038/s41598-019-
712 39679-0.
- 713 25. Sung, B.H., Ketova, T., Hoshino, D., Zijlstra, A., and Weaver, A.M. (2015). Directional cell movement through
714 tissues is controlled by exosome secretion. *Nat Commun* 6, 7164. 10.1038/ncomms8164.
- 715 26. Fordjour, F.K., Abuelreich, S., Hong, X., Chatterjee, E., Lallai, V., Ng, M., Saftics, A., Deng, F., Carnel-Amar,
716 N., Wakimoto, H., et al. (2023). Exomap1 mouse: a transgenic model for in vivo studies of exosome biology.
717 bioRxiv. 10.1101/2023.05.29.542707.
- 718 27. Nikoloff, J.M., Saucedo-Espinosa, M.A., Kling, A., and Dittrich, P.S. (2021). Identifying extracellular vesicle
719 populations from single cells. *Proc Natl Acad Sci U S A* 118. 10.1073/pnas.2106630118.
- 720 28. Giraldez, M.D., Spengler, R.M., Etheridge, A., Godoy, P.M., Barczak, A.J., Srinivasan, S., De Hoff, P.L.,
721 Tanriverdi, K., Courtright, A., Lu, S., et al. (2018). Comprehensive multi-center assessment of small RNA-seq
722 methods for quantitative miRNA profiling. *Nat Biotechnol* 36, 746-757. 10.1038/nbt.4183.
- 723 29. Sung, B.H., and Weaver, A.M. (2023). Visualization of Exosome Release and Uptake During Cell Migration
724 Using the Live Imaging Reporter pHluorin_M153R-CD63. *Methods Mol Biol* 2608, 83-96. 10.1007/978-1-
725 0716-2887-4_6.
- 726 30. Blandin, A., Amosse, J., Froger, J., Hilairret, G., Durcin, M., Fizanne, L., Ghesquiere, V., Prieur, X., Chaigneau,
727 J., Vergori, L., et al. (2023). Extracellular vesicles are carriers of adiponectin with insulin-sensitizing and anti-
728 inflammatory properties. *Cell Rep* 42, 112866. 10.1016/j.celrep.2023.112866.
- 729 31. Daley, J.M., Brancato, S.K., Thomay, A.A., Reichner, J.S., and Albina, J.E. (2010). The phenotype of murine
730 wound macrophages. *J Leukoc Biol* 87, 59-67. 10.1189/jlb.0409236.
- 731 32. Rani, M., and Schwacha, M.G. (2017). The composition of T-cell subsets are altered in the burn wound early
732 after injury. *PLoS One* 12, e0179015. 10.1371/journal.pone.0179015.
- 733 33. Engin, A.B. (2017). Adipocyte-Macrophage Cross-Talk in Obesity. *Adv Exp Med Biol* 960, 327-343.
734 10.1007/978-3-319-48382-5_14.
- 735 34. Ellett, F., Pazhakh, V., Pase, L., Benard, E.L., Weerasinghe, H., Azabdaftari, D., Alasmari, S., Andrianopoulos,
736 A., and Lieschke, G.J. (2018). Macrophages protect *Talaromyces marneffe* conidia from myeloperoxidase-
737 dependent neutrophil fungicidal activity during infection establishment in vivo. *PLoS Pathog* 14, e1007063.
738 10.1371/journal.ppat.1007063.
- 739 35. Wang, S., Song, R., Wang, Z., Jing, Z., Wang, S., and Ma, J. (2018). S100A8/A9 in Inflammation. *Front*
740 *Immunol* 9, 1298. 10.3389/fimmu.2018.01298.
- 741 36. Wei, J., and Gronert, K. (2019). Eicosanoid and Specialized Proresolving Mediator Regulation of Lymphoid
742 Cells. *Trends Biochem Sci* 44, 214-225. 10.1016/j.tibs.2018.10.007.
- 743 37. Pan, R.Y., Chu, M.T., Wang, C.W., Lee, Y.S., Lemonnier, F., Michels, A.W., Schutte, R., Ostrov, D.A., Chen,
744 C.B., Phillips, E.J., et al. (2019). Identification of drug-specific public TCR driving severe cutaneous adverse
745 reactions. *Nat Commun* 10, 3569. 10.1038/s41467-019-11396-2.

- 746 38. Wang, X., Balaji, S., Steen, E.H., Li, H., Rae, M.M., Blum, A.J., Miao, Q., Butte, M.J., Bollyky, P.L., and
747 Keswani, S.G. (2019). T Lymphocytes Attenuate Dermal Scarring by Regulating Inflammation,
748 Neovascularization, and Extracellular Matrix Remodeling. *Adv Wound Care (New Rochelle)* 8, 527-537.
749 10.1089/wound.2019.0981.
- 750 39. Amon, L., Lehmann, C.H.K., Baranska, A., Schoen, J., Heger, L., and Dudziak, D. (2019). Transcriptional
751 control of dendritic cell development and functions. *Int Rev Cell Mol Biol* 349, 55-151.
752 10.1016/bs.ircmb.2019.10.001.
- 753 40. Johnson, J., Jaggars, R.M., Gopalkrishna, S., Dahdah, A., Murphy, A.J., Hanssen, N.M.J., and Nagareddy, P.R.
754 (2022). Oxidative Stress in Neutrophils: Implications for Diabetic Cardiovascular Complications. *Antioxid*
755 *Redox Signal* 36, 652-666. 10.1089/ars.2021.0116.
- 756 41. Hong, W., Yang, B., He, Q., Wang, J., and Weng, Q. (2022). New Insights of CCR7 Signaling in Dendritic Cell
757 Migration and Inflammatory Diseases. *Front Pharmacol* 13, 841687. 10.3389/fphar.2022.841687.
- 758 42. Kim, K., Park, S.E., Park, J.S., and Choi, J.H. (2022). Characteristics of plaque lipid-associated macrophages
759 and their possible roles in the pathogenesis of atherosclerosis. *Curr Opin Lipidol* 33, 283-288.
760 10.1097/MOL.0000000000000842.
- 761 43. Deming, Y., Filipello, F., Cignarella, F., Cantoni, C., Hsu, S., Mikesell, R., Li, Z., Del-Aguila, J.L., Dube, U.,
762 Farias, F.G., et al. (2019). The MS4A gene cluster is a key modulator of soluble TREM2 and Alzheimer's
763 disease risk. *Sci Transl Med* 11. 10.1126/scitranslmed.aau2291.
- 764 44. Guo, L., Liu, Y., Chen, Y., Xu, J., and Liu, Y. (2023). Liver macrophages show an immunotolerance phenotype
765 in nonalcoholic fatty liver combined with *Porphyromonas gingivalis*-lipopolysaccharide infection. *Hua Xi Kou*
766 *Qiang Yi Xue Za Zhi* 41, 385-394. 10.7518/hxkq.2023.2023111.
- 767 45. Boing, A.N., van der Pol, E., Grootemaat, A.E., Coumans, F.A., Sturk, A., and Nieuwland, R. (2014). Single-
768 step isolation of extracellular vesicles by size-exclusion chromatography. *J Extracell Vesicles* 3.
769 10.3402/jev.v3.23430.
- 770 46. Sodar, B.W., Kittel, A., Paloczi, K., Vukman, K.V., Osteikoetxea, X., Szabo-Taylor, K., Nemeth, A., Sperlagh,
771 B., Baranyai, T., Giricz, Z., et al. (2016). Low-density lipoprotein mimics blood plasma-derived exosomes and
772 microvesicles during isolation and detection. *Sci Rep* 6, 24316. 10.1038/srep24316.
- 773 47. McFarland-Mancini, M.M., Funk, H.M., Paluch, A.M., Zhou, M., Giridhar, P.V., Mercer, C.A., Kozma, S.C.,
774 and Drew, A.F. (2010). Differences in wound healing in mice with deficiency of IL-6 versus IL-6 receptor. *J*
775 *Immunol* 184, 7219-7228. 10.4049/jimmunol.0901929.
- 776 48. LeBlanc, S., Arabzadeh, A., Benlolo, S., Breton, V., Turbide, C., Beauchemin, N., and Nouvion, A.L. (2011).
777 CEACAM1 deficiency delays important wound healing processes. *Wound Repair Regen* 19, 745-752.
778 10.1111/j.1524-475X.2011.00742.x.
- 779 49. Bourke, C.D., Prendergast, C.T., Sanin, D.E., Oulton, T.E., Hall, R.J., and Mountford, A.P. (2015). Epidermal
780 keratinocytes initiate wound healing and pro-inflammatory immune responses following percutaneous
781 schistosome infection. *Int J Parasitol* 45, 215-224. 10.1016/j.ijpara.2014.11.002.

- 782 50. Shapira, S., Ben-Amotz, O., Sher, O., Kazanov, D., Mashiah, J., Kraus, S., Gur, E., and Arber, N. (2015).
783 Delayed Wound Healing in Heat Stable Antigen (HSA/CD24)-Deficient Mice. *PLoS One* *10*, e0139787.
784 10.1371/journal.pone.0139787.
- 785 51. Huang, X., Gu, S., Liu, C., Zhang, L., Zhang, Z., Zhao, Y., Khoong, Y., Li, H., Gao, Y., Liu, Y., et al. (2022).
786 CD39(+) Fibroblasts Enhance Myofibroblast Activation by Promoting IL-11 Secretion in Hypertrophic Scars.
787 *J Invest Dermatol* *142*, 1065-1076 e1019. 10.1016/j.jid.2021.07.181.
- 788 52. Noguchi, F., Nakajima, T., Inui, S., Reddy, J.K., and Itami, S. (2014). Alteration of skin wound healing in
789 keratinocyte-specific mediator complex subunit 1 null mice. *PLoS One* *9*, e102271.
790 10.1371/journal.pone.0102271.
- 791 53. Prabhu, V., Rao, B.S.S., Rao, A.C.K., Prasad, K., and Mahato, K.K. (2022). Photobiomodulation invigorating
792 collagen deposition, proliferating cell nuclear antigen and Ki67 expression during dermal wound repair in
793 mice. *Lasers Med Sci* *37*, 171-180. 10.1007/s10103-020-03202-z.
- 794 54. Wang, L., Jiang, J., Zhou, T., Xue, X., and Cao, Y. (2021). Improvement of Cerebral Ischemia-Reperfusion
795 Injury via Regulation of Apoptosis by Exosomes Derived from BDNF-Overexpressing HEK293. *Biomed Res*
796 *Int* *2021*, 6613510. 10.1155/2021/6613510.
- 797 55. Wang, C., Li, N., Li, Y., Hou, S., Zhang, W., Meng, Z., Wang, S., Jia, Q., Tan, J., Wang, R., et al. (2022).
798 Engineering a HEK-293T exosome-based delivery platform for efficient tumor-targeting
799 chemotherapy/internal irradiation combination therapy. *J Nanobiotechnology* *20*, 247. 10.1186/s12951-022-
800 01462-1.
- 801 56. Zhang, J., Song, H., Dong, Y., Li, G., Li, J., Cai, Q., Yuan, S., Wang, Y., and Song, H. (2023). Surface
802 Engineering of HEK293 Cell-Derived Extracellular Vesicles for Improved Pharmacokinetic Profile and
803 Targeted Delivery of IL-12 for the Treatment of Hepatocellular Carcinoma. *Int J Nanomedicine* *18*, 209-223.
804 10.2147/IJN.S388916.
- 805 57. Qu, Y., Zhang, Q., Cai, X., Li, F., Ma, Z., Xu, M., and Lu, L. (2017). Exosomes derived from miR-181-5p-
806 modified adipose-derived mesenchymal stem cells prevent liver fibrosis via autophagy activation. *J Cell Mol*
807 *Med* *21*, 2491-2502. 10.1111/jcmm.13170.
- 808 58. Katakowski, M., Buller, B., Zheng, X., Lu, Y., Rogers, T., Osobamiro, O., Shu, W., Jiang, F., and Chopp, M.
809 (2013). Exosomes from marrow stromal cells expressing miR-146b inhibit glioma growth. *Cancer Lett* *335*,
810 201-204. 10.1016/j.canlet.2013.02.019.
- 811 59. Wang, Q., Zhu, G., Cao, X., Dong, J., Song, F., and Niu, Y. (2017). Blocking AGE-RAGE Signaling Improved
812 Functional Disorders of Macrophages in Diabetic Wound. *J Diabetes Res* *2017*, 1428537.
813 10.1155/2017/1428537.
- 814 60. Fernandes, H., Zonnari, A., Abreu, R., Aday, S., Barao, M., Albino, I., Lino, M., Branco, A., Seabra, C.,
815 Barata, T., et al. (2022). Extracellular vesicles enriched with an endothelial cell pro-survival microRNA affects
816 skin tissue regeneration. *Mol Ther Nucleic Acids* *28*, 307-327. 10.1016/j.omtn.2022.03.018.

- 817 61. de Almeida Oliveira, N.C., Neri, E.A., Silva, C.M., Valadao, I.C., Fonseca-Alaniz, M.H., Zogbi, C., Levy, D.,
818 Bydlowski, S.P., and Krieger, J.E. (2022). Multicellular regulation of miR-196a-5p and miR-425-5 from
819 adipose stem cell-derived exosomes and cardiac repair. *Clin Sci (Lond)* *136*, 1281-1301.
820 10.1042/CS20220216.
- 821 62. Kwon, D.N., Chang, B.S., and Kim, J.H. (2014). MicroRNA dysregulation in liver and pancreas of CMP-
822 Neu5Ac hydroxylase null mice disrupts insulin/PI3K-AKT signaling. *Biomed Res Int* *2014*, 236385.
823 10.1155/2014/236385.
- 824 63. Yuan, J., Wu, Y., Li, L., and Liu, C. (2020). MicroRNA-425-5p promotes tau phosphorylation and cell
825 apoptosis in Alzheimer's disease by targeting heat shock protein B8. *J Neural Transm (Vienna)* *127*, 339-346.
826 10.1007/s00702-019-02134-5.
- 827 64. Lou, G., Song, X., Yang, F., Wu, S., Wang, J., Chen, Z., and Liu, Y. (2015). Exosomes derived from miR-122-
828 modified adipose tissue-derived MSCs increase chemosensitivity of hepatocellular carcinoma. *J Hematol*
829 *Oncol* *8*, 122. 10.1186/s13045-015-0220-7.
- 830 65. Lee, H.K., Lee, B.R., Lee, T.J., Lee, C.M., Li, C., O'Connor, P.M., Dong, Z., and Kwon, S.H. (2022).
831 Differential release of extracellular vesicle tRNA from oxidative stressed renal cells and ischemic kidneys. *Sci*
832 *Rep* *12*, 1646. 10.1038/s41598-022-05648-3.
- 833 66. Spiegel, A., Brooks, M.W., Houshyar, S., Reinhardt, F., Ardolino, M., Fessler, E., Chen, M.B., Krall, J.A.,
834 DeCock, J., Zervantonakis, I.K., et al. (2016). Neutrophils Suppress Intraluminal NK Cell-Mediated Tumor
835 Cell Clearance and Enhance Extravasation of Disseminated Carcinoma Cells. *Cancer Discov* *6*, 630-649.
836 10.1158/2159-8290.CD-15-1157.
- 837 67. Achari, A.E., and Jain, S.K. (2017). Adiponectin, a Therapeutic Target for Obesity, Diabetes, and Endothelial
838 Dysfunction. *Int J Mol Sci* *18*. 10.3390/ijms18061321.
- 839 68. Yanai, H., and Yoshida, H. (2019). Beneficial Effects of Adiponectin on Glucose and Lipid Metabolism and
840 Atherosclerotic Progression: Mechanisms and Perspectives. *Int J Mol Sci* *20*. 10.3390/ijms20051190.
- 841 69. Lou, R., Chen, J., Zhou, F., Wang, C., Leung, C.H., and Lin, L. (2022). Exosome-cargoed microRNAs:
842 Potential therapeutic molecules for diabetic wound healing. *Drug Discov Today* *27*, 103323.
843 10.1016/j.drudis.2022.07.008.
- 844 70. Barman, B., Sung, B.H., Krystofiak, E., Ping, J., Ramirez, M., Millis, B., Allen, R., Prasad, N., Chetyrkin, S.,
845 Calcutt, M.W., et al. (2022). VAP-A and its binding partner CERT drive biogenesis of RNA-containing
846 extracellular vesicles at ER membrane contact sites. *Dev Cell* *57*, 974-994 e978.
847 10.1016/j.devcel.2022.03.012.
- 848 71. Tang, Y., Yang, L.J., Liu, H., Song, Y.J., Yang, Q.Q., Liu, Y., Qian, S.W., and Tang, Q.Q. (2023). Exosomal
849 miR-27b-3p secreted by visceral adipocytes contributes to endothelial inflammation and atherogenesis. *Cell*
850 *Rep* *42*, 111948. 10.1016/j.celrep.2022.111948.
- 851 72. Turk, M.A., Chung, C.Z., Manni, E., Zukowski, S.A., Engineer, A., Badakhshi, Y., Bi, Y., and Heinemann, I.U.
852 (2018). MiRAR-miRNA Activity Reporter for Living Cells. *Genes (Basel)* *9*. 10.3390/genes9060305.

- 853 73. Ying, W., Riopel, M., Bandyopadhyay, G., Dong, Y., Birmingham, A., Seo, J.B., Ofrecio, J.M., Wollam, J.,
854 Hernandez-Carretero, A., Fu, W., et al. (2017). Adipose Tissue Macrophage-Derived Exosomal miRNAs Can
855 Modulate In Vivo and In Vitro Insulin Sensitivity. *Cell* *171*, 372-384 e312. 10.1016/j.cell.2017.08.035.
- 856 74. Albanese, M., Chen, Y.A., Huls, C., Gartner, K., Tagawa, T., Mejias-Perez, E., Keppler, O.T., Gobel, C.,
857 Zeidler, R., Shein, M., et al. (2021). MicroRNAs are minor constituents of extracellular vesicles that are rarely
858 delivered to target cells. *PLoS Genet* *17*, e1009951. 10.1371/journal.pgen.1009951.
- 859 75. Chevillet, J.R., Kang, Q., Ruf, I.K., Briggs, H.A., Vojtech, L.N., Hughes, S.M., Cheng, H.H., Arroyo, J.D.,
860 Meredith, E.K., Gallichotte, E.N., et al. (2014). Quantitative and stoichiometric analysis of the microRNA
861 content of exosomes. *Proc Natl Acad Sci U S A* *111*, 14888-14893. 10.1073/pnas.1408301111.
- 862 76. Qi, R., Wang, J., Wang, Q., Qiu, X., Yang, F., Liu, Z., and Huang, J. (2019). MicroRNA-425 controls
863 lipogenesis and lipolysis in adipocytes. *Biochim Biophys Acta Mol Cell Biol Lipids* *1864*, 744-755.
864 10.1016/j.bbalip.2019.02.007.
- 865 77. Sung, B.H., von Lersner, A., Guerrero, J., Krystofiak, E.S., Inman, D., Pelletier, R., Zijlstra, A., Ponik, S.M.,
866 and Weaver, A.M. (2020). A live cell reporter of exosome secretion and uptake reveals pathfinding behavior of
867 migrating cells. *Nat Commun* *11*, 2092. 10.1038/s41467-020-15747-2.
- 868 78. de Jong, O.G., Murphy, D.E., Mager, I., Willms, E., Garcia-Guerra, A., Gitz-Francois, J.J., Lefferts, J., Gupta,
869 D., Steenbeek, S.C., van Rheenen, J., et al. (2020). A CRISPR-Cas9-based reporter system for single-cell
870 detection of extracellular vesicle-mediated functional transfer of RNA. *Nat Commun* *11*, 1113.
871 10.1038/s41467-020-14977-8.
- 872 79. Einhauer, A., and Jungbauer, A. (2001). The FLAG peptide, a versatile fusion tag for the purification of
873 recombinant proteins. *J Biochem Biophys Methods* *49*, 455-465. 10.1016/s0165-022x(01)00213-5.
- 874 80. Fajardo, R.J., Karim, L., Calley, V.I., and Bouxsein, M.L. (2014). A review of rodent models of type 2 diabetic
875 skeletal fragility. *J Bone Miner Res* *29*, 1025-1040. 10.1002/jbmr.2210.
- 876 81. Lee, Y., Berglund, E.D., Yu, X., Wang, M.Y., Evans, M.R., Scherer, P.E., Holland, W.L., Charron, M.J., Roth,
877 M.G., and Unger, R.H. (2014). Hyperglycemia in rodent models of type 2 diabetes requires insulin-resistant
878 alpha cells. *Proc Natl Acad Sci U S A* *111*, 13217-13222. 10.1073/pnas.1409638111.
- 879 82. Thery, C., Witwer, K.W., Aikawa, E., Alcaraz, M.J., Anderson, J.D., Andriantsitohaina, R., Antoniou, A., Arab,
880 T., Archer, F., Atkin-Smith, G.K., et al. (2018). Minimal information for studies of extracellular vesicles 2018
881 (MISEV2018): a position statement of the International Society for Extracellular Vesicles and update of the
882 MISEV2014 guidelines. *J Extracell Vesicles* *7*, 1535750. 10.1080/20013078.2018.1535750.
- 883 83. Welsh, J.A., Van Der Pol, E., Arksteijn, G.J.A., Bremer, M., Brisson, A., Coumans, F., Dignat-George, F.,
884 Duggan, E., Ghiran, I., Giebel, B., et al. (2020). MIFlowCyt-EV: a framework for standardized reporting of
885 extracellular vesicle flow cytometry experiments. *J Extracell Vesicles* *9*, 1713526.
886 10.1080/20013078.2020.1713526.

- 887 84. Shpigelman, J., Lao, F.S., Yao, S., Li, C., Saito, T., Sato-Kaneko, F., Nolan, J.P., Shukla, N.M., Pu, M., Messer,
888 K., et al. (2021). Generation and Application of a Reporter Cell Line for the Quantitative Screen of
889 Extracellular Vesicle Release. *Front Pharmacol* *12*, 668609. 10.3389/fphar.2021.668609.
- 890 85. Welsh, J.A., Arkesteijn, G.J.A., Bremer, M., Cimorelli, M., Dignat-George, F., Giebel, B., Gorgens, A.,
891 Hendrix, A., Kuiper, M., Lacroix, R., et al. (2023). A compendium of single extracellular vesicle flow
892 cytometry. *J Extracell Vesicles* *12*, e12299. 10.1002/jev2.12299.
- 893 86. Li, M., Wang, T., Tian, H., Wei, G., Zhao, L., and Shi, Y. (2019). Macrophage-derived exosomes accelerate
894 wound healing through their anti-inflammation effects in a diabetic rat model. *Artif Cells Nanomed Biotechnol*
895 *47*, 3793-3803. 10.1080/21691401.2019.1669617.
- 896 87. Hsu, H.H., Wang, A.Y.L., Loh, C.Y.Y., Pai, A.A., and Kao, H.K. (2022). Therapeutic Potential of Exosomes
897 Derived from Diabetic Adipose Stem Cells in Cutaneous Wound Healing of db/db Mice. *Pharmaceutics* *14*.
898 10.3390/pharmaceutics14061206.
- 899 88. Love, M.I., Huber, W., and Anders, S. (2014). Moderated estimation of fold change and dispersion for RNA-
900 seq data with DESeq2. *Genome Biol* *15*, 550. 10.1186/s13059-014-0550-8.
- 901 89. Sahraeian, S.M.E., Mohiyuddin, M., Sebra, R., Tilgner, H., Afshar, P.T., Au, K.F., Bani Asadi, N., Gerstein,
902 M.B., Wong, W.H., Snyder, M.P., et al. (2017). Gaining comprehensive biological insight into the
903 transcriptome by performing a broad-spectrum RNA-seq analysis. *Nat Commun* *8*, 59. 10.1038/s41467-017-
904 00050-4.
- 905 90. Ye, Z., Wang, S., Huang, X., Chen, P., Deng, L., Li, S., Lin, S., Wang, Z., and Liu, B. (2022). Plasma
906 Exosomal miRNAs Associated With Metabolism as Early Predictor of Gestational Diabetes Mellitus. *Diabetes*
907 *71*, 2272-2283. 10.2337/db21-0909.

List of Figure Captions**Figure 1. Diabetic obese mice drive a transcriptional reprogramming of immune cell subsets recruited into sites of cutaneous injury.**

(A) Schematic of PVA implant model for the harvest of EVs from cutaneous site. (B) scRNAseq of cells from PVA sponge implants in WT vs. db/db mice (C) Expression of genesets mapping to macrophages, neutrophils, dendritic cells (DCs), and lymphocytes based on supporting references in Table S1. (D) Analysis of changes in gene expression of top 10 up-regulated vs. down-regulated genes in cells from WT vs. db/db donors (GSE #242496).

Figure 2. Identification and characterization of EVs derived from the PVA sponges.

(A) Schematic of EV purification and profiling using size exclusion chromatography (SEC). (B) Quantification of SEC fractions by determining EV concentration using vFRed staining as detailed in the Materials and Methods (bars) and soluble protein using a BCA assay (line) from a representative WT EV sample. EV concentration of WT vs. db/db EVs from each SEC fraction is quantified in replicates in Supplementary Figure S2A. (C) Immunoblotting of SEC fractions to detect CD9 (bottom) and a Memcode protein stain (top) for total protein from each SEC fraction. (D) Immunoblotting of EV markers of whole cell lysates (WCLs) and EVs from a representative WT PVA donor. (E) Blood glucose and (F) body weight measurements that define the pathophysiology of the db/db mouse model. (G) EV concentration and (H) size distributions of WT vs. db/db EVs in fraction 7 (n=10). (p values: * <0.05 , **** <0.0001).

Figure 3. vFC of EVs isolated from PVA sponge implants.

(A) Schematic of EV analyses by batch vs. vesicle flow cytometry (vFC). (B) Quantification of a bead-based EV protein screen of inflammation-related proteins of WT EVs. (C) Representative vFC analysis of isotype and tetraspanin levels on WT PVA EVs, and (D) immune-related proteins. vFC analysis of WT vs. db/db EVs for (E) tetraspanins, (F) integrins, (G) immune-related proteins, and (H) other EV-related inflammation proteins. (n=5 for each group; p values: ** <0.005 , * <0.05).

936 **Figure 4. Adoptive transfer of EVs from diabetic obese donors have impaired wound healing activity.**

937 (A) Schematic of EV adoptive transfer strategy. (B) Representative images of recipient wound beds on each day after
 938 treatment with saline control, WT EVs, or db/db EVs (a volume of 50 μL of EVs at $5\text{-}7 \times 10^6$ PVA EVs/ μL) and (C)
 939 quantification of wound closure kinetics (n=10 per group; p values: ****<0.0001, **<0.005, *<0.05). (D) Representative
 940 hematoxylin and eosin (H&E) stained wounds on Day 14 after treatment with WT vs. db/db EVs (inset on right = high
 941 magnification). (E) Quantification of epidermis thickness (μm) based on H&E images indicated with brackets in Panel
 942 D. (F) Quantification of cell count per area (mm^2) based on H&E-stained images. (G) Localization of Ki67⁺ cells by
 943 immunohistochemistry on Day 14 after treatment with WT or db/db EVs. (H) Schematic of WT CD63 and CD63-FLAG
 944 tag (top) and vFC analysis of surface levels FLAG tag (bottom). (I) Immunoblotting to detect FLAG tag expression. (J)
 945 Localization of FLAG-tagged EVs in wound bed after a 24 hour treatment with saline (top), CD63-expressing EVs
 946 (middle), or CD63-FLAG expressing EVs. (green line: edge, blue box: wound margin, red box: wound bed). High
 947 magnification images of wound margin (middle) and wound bed (red) are shown. (K) Uptake of control CD63 (top) vs.
 948 CD63-FLAG-tagged (bottom) EVs into MEFs. (L) Quantification of FLAG-tagged EV uptake into MEFs.

949
 950 **Figure 5. Regulation of miRNA EV payloads isolated in diabetic obese mouse model.**

951 (A) miRNAseq analysis of fold changes in WT vs db/db EVs. (B) Distribution of miRNA profile between WT and db/db
 952 EVs. (C) Analysis of fold change (FC) vs. significance (P) of miRNAs identified as described in the Materials and
 953 Methods. (D) KEGG pathway analysis of miRNAs identified. (E) Schematic of EV collection from cultured sponge-
 954 derived macrophages. (F) Quantification of EV yield from cultured macrophages. (G) qRT-PCR analysis of miR-425-
 955 5p in EVs isolated from the conditioned media from db/db vs. WT macrophages (n=3 from each group. p < 0.005).

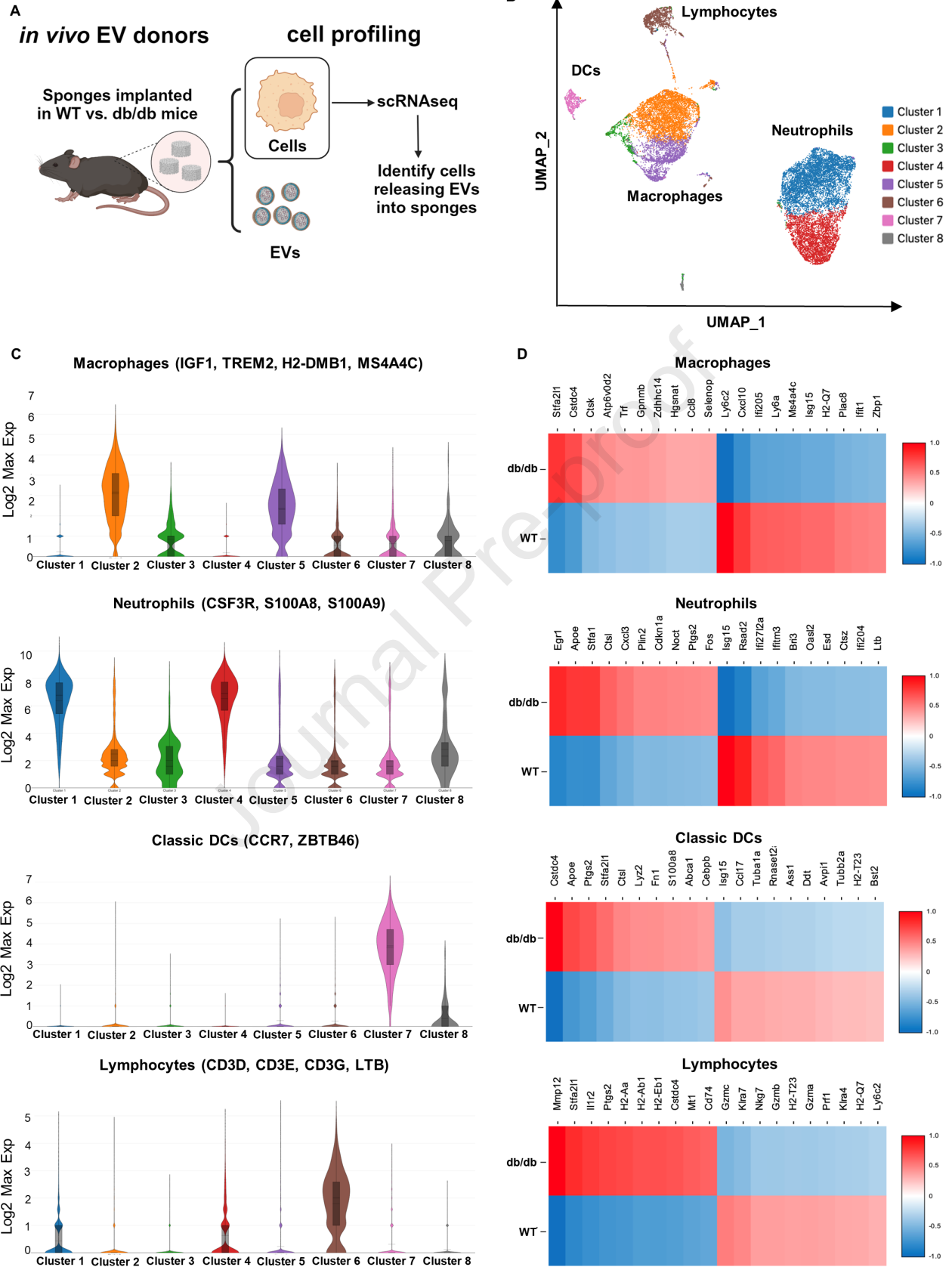
956
 957 **Figure 6. Biological testing of miR-425-5p-loaded EVs.**

958 (A) Schematic of EV collection, loading with specific miRNAs *in vitro*, followed by treatment of splinted wounds *in*
 959 *vivo* to assess miR-425-5p biological activity. (B) Comparison of wound closure kinetics of normal WT EVs (i.e., no
 960 miRNA loading) vs. WT EVs loaded with miR-425-5p to show that EVs loaded with miR-425-5p are more pro-reparative
 961 than WT EVs. (C) Analysis of wound closure kinetics with controls including saline (black), mock-treated EVs (i.e., EVs
 962 treated with Exofect reagent without miRNA; green), negative control miRNA-loaded EVs (i.e., cel-miR-67; blue), or

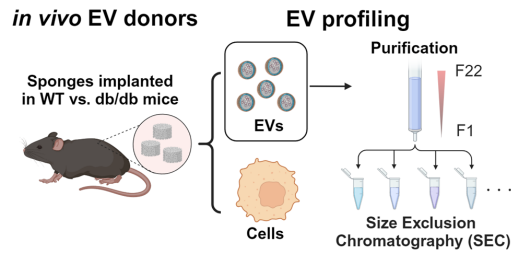
963 miR-425-5p-loaded EVs (red) (a volume of 50 μL of EVs at $5\text{-}7 \times 10^6$ PVA EVs/ μL). (D) Localization and (E)
964 quantification of Ki67⁺ cells in the basal epidermal skin layer to assess the general pro-reparative effects of miR-425-5p-
965 loaded EV treatment. (F) Representative H&E (top) and Masson's Trichrome stained images (bottom) on Day 14 after
966 treatment with saline, neg-miRNA-loaded EVs or miR-425-5p-loaded EVs (Red dotted line = wound margin; blue box
967 = area used for cell counts and epidermis thickness measurements). Quantification of the effects of treatment with neg-
968 miRNA-loaded EVs vs. miR-425-5p-loaded EVs on (G) cell count, (H) epidermis thickness, and (I) collagen as a
969 percentage of the dermis area (mm^2) based on Masson's Trichrome staining. (J) Protein panel quantifying changes in
970 adipokine/cytokine expression in wound beds treated with miR-425-5p-loaded EVs vs. negative control miRNA-loaded
971 EVs at 14 days (n=2 for each treatment group). Supplementary Figure S8 has the complete profile. (K) Schematic of *in*
972 *vitro* of PVA sponge-derived EVs loaded with negative control miRNA vs. miR-425-5p used to treat MEFs. (L)
973 Immunoblotting of Adiponectin protein of MEFs treated with control vs. miR-425-5p-loaded EVs. (p values:
974 ****<0.0001, ***<0.001, **<0.005, *<0.05)

975
976 **Figure 7. Transgenic mice expressing the tetraspanin CD9-GFP to assess cell type specific EV release and track**
977 **EV uptake.**

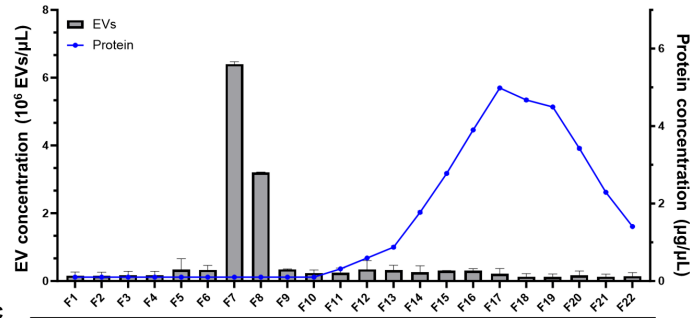
978 (A) Schematic of lineage mapping mouse lines using CD9-GFP TIGER model and cell-type specific expression of Cre.
979 (B) Analysis of GFP expression in cells and (C) EVs from PVA sponge implants from transgenic mice expressing CD9-
980 GFP under the control of LysM, TEK, or Krt14 promoters, as detailed in the Materials and Methods. (D) Schematic of
981 adoptive transfer of CD9-GFP EVs into splinted wounds of db/db mice. (a volume of 50 μL of EVs at $5\text{-}7 \times 10^6$ PVA
982 EVs/ μL) (E) Detection of CD9-GFP⁺ EVs (left; green fluorescence) vs. WT EVs (right; non-fluorescent EVs from CD9-
983 GFP⁻ mice) in the wound bed. Representative low magnification images of (F) WT non-fluorescent EVs vs. (G) CD9-
984 GFP⁺ EVs (white arrowheads) in the splinted wound (left and right images comprise the full wound site), counterstained
985 with vimentin for fibroblasts (red) and DAPI for nuclei (blue). (H) Representative high magnification images of CD9-
986 GFP⁺ EVs from two different fields (top and bottom) detected in the wound margin (based on red box from Panel D) and
987 (I) wound bed (based on blue box from Panel D). CD9-GFP⁺ EVs colocalized with vimentin indicated with white arrows.



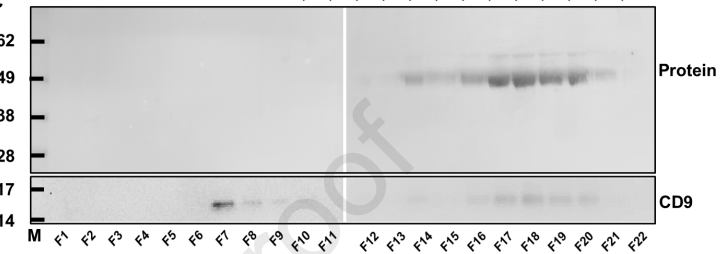
A



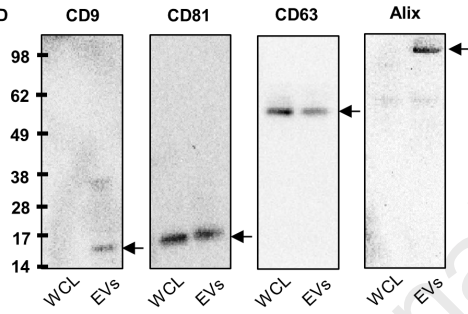
B



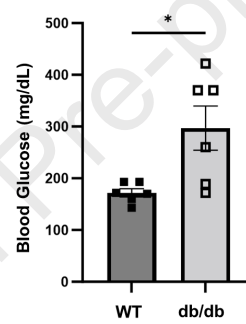
C



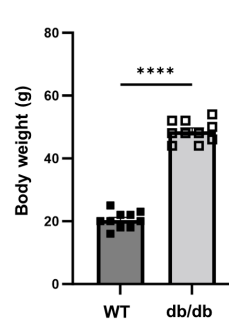
D



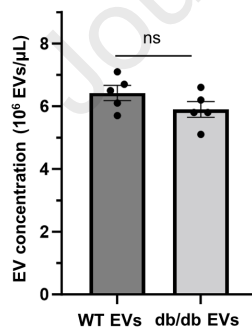
E



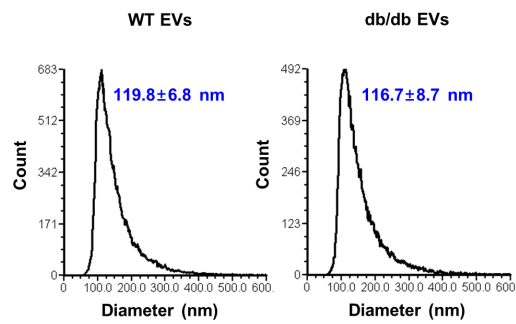
F

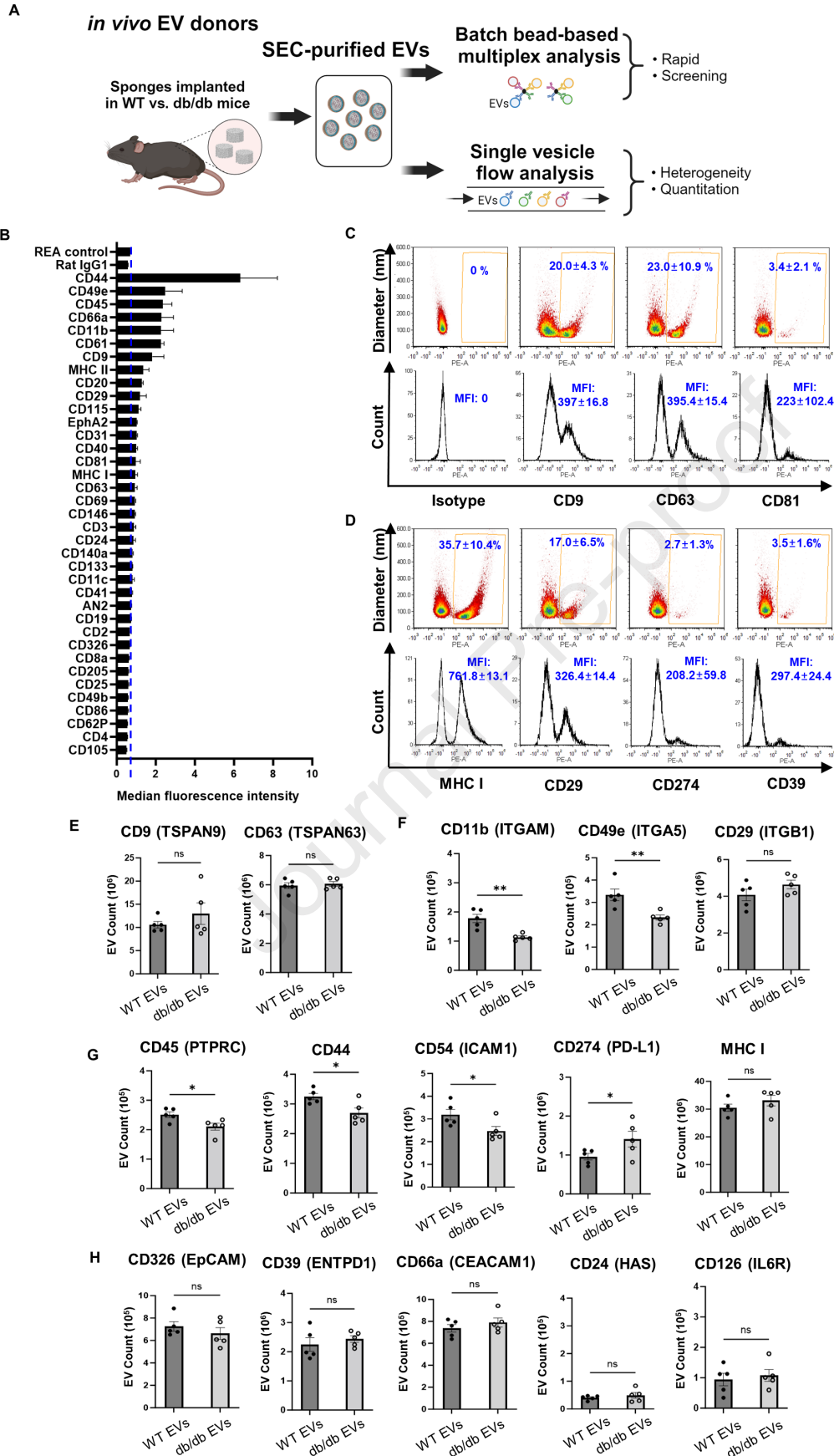


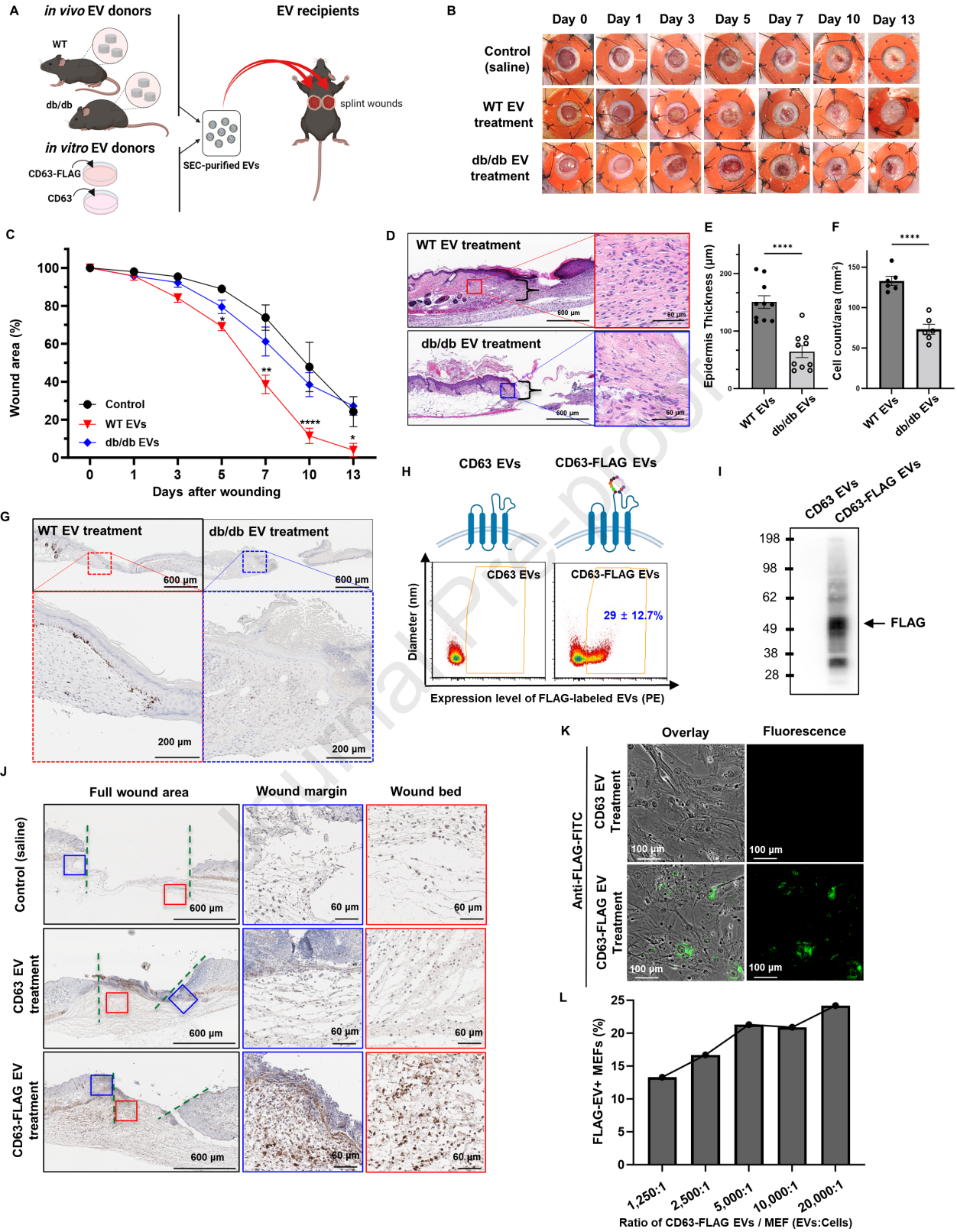
G



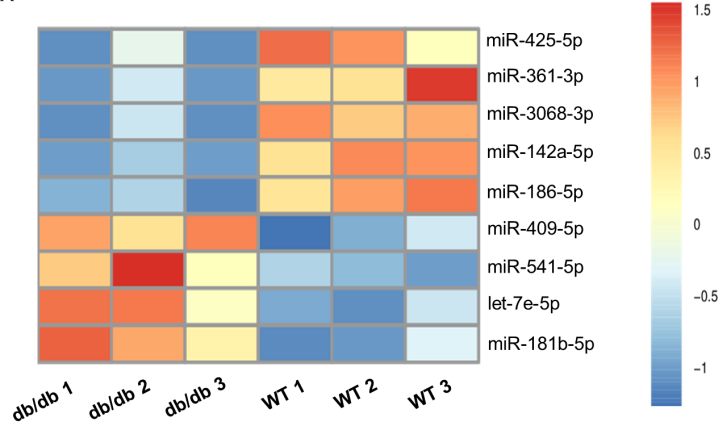
H



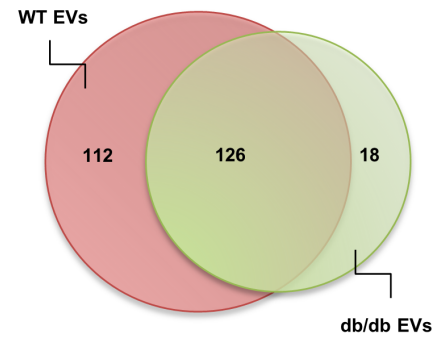




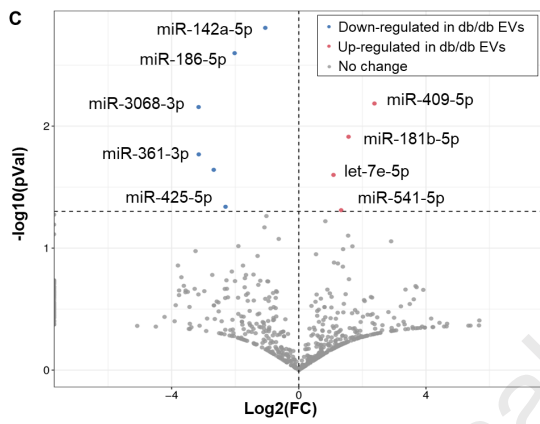
A



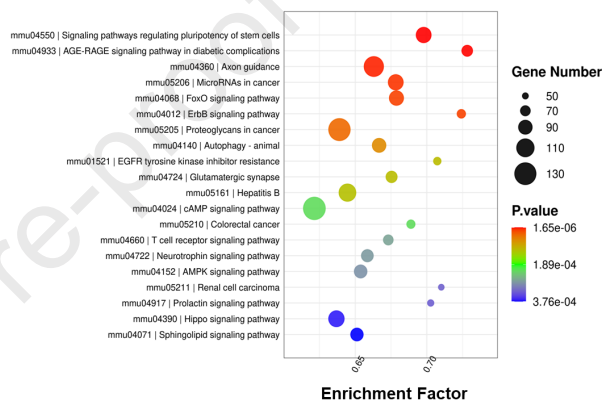
B



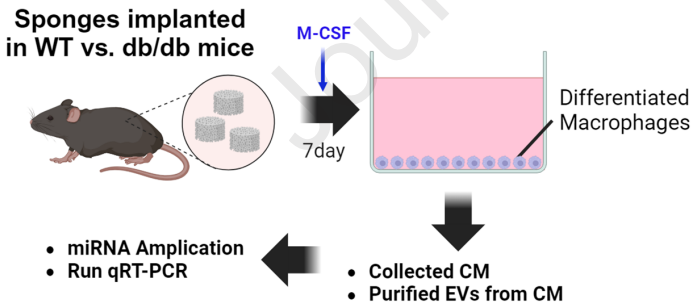
C



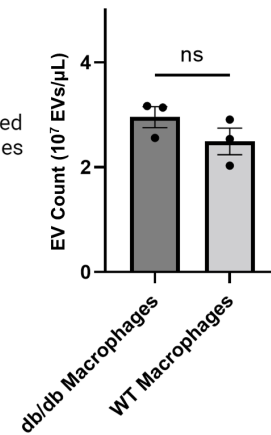
D



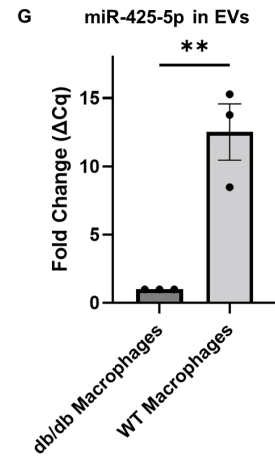
E

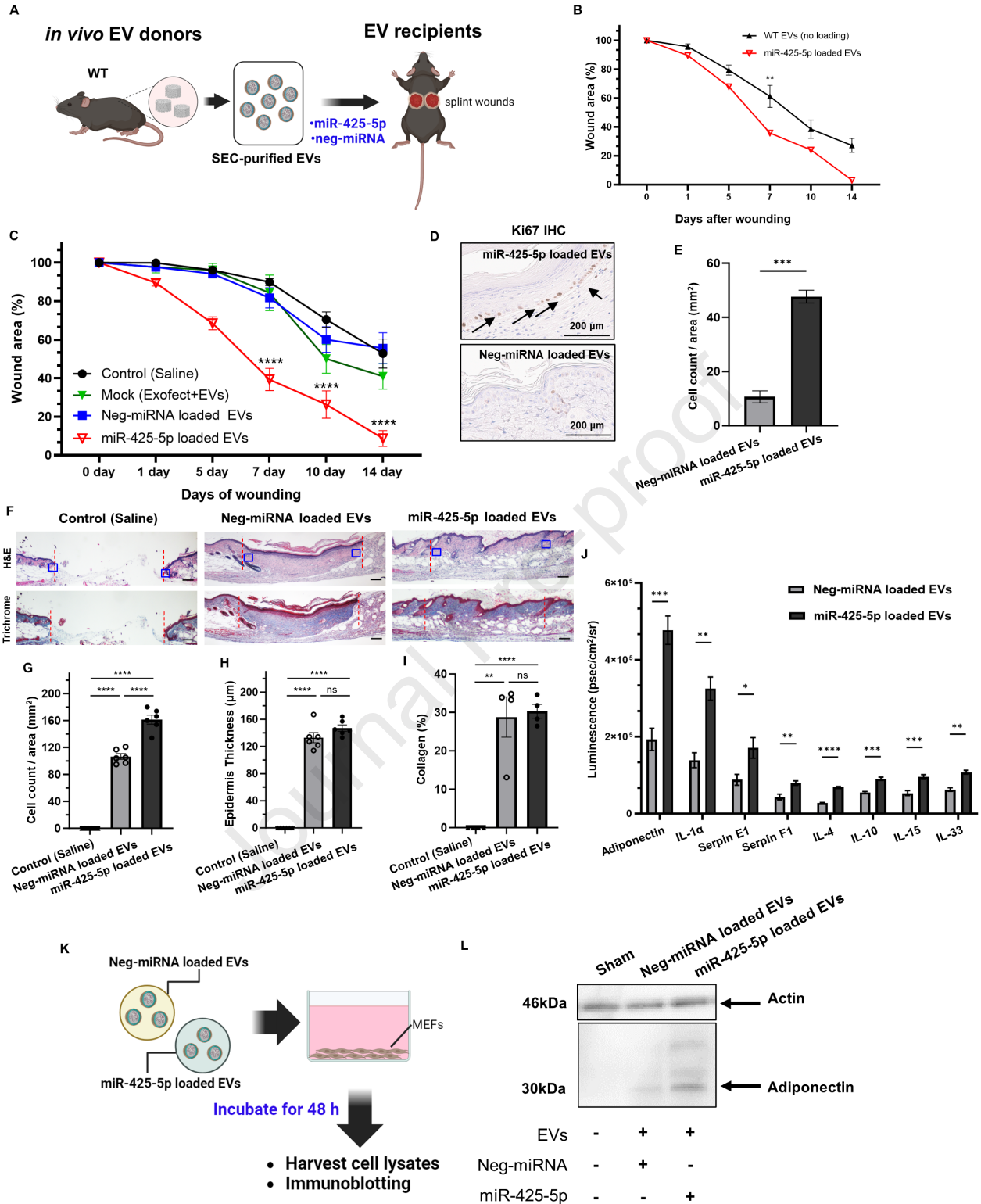


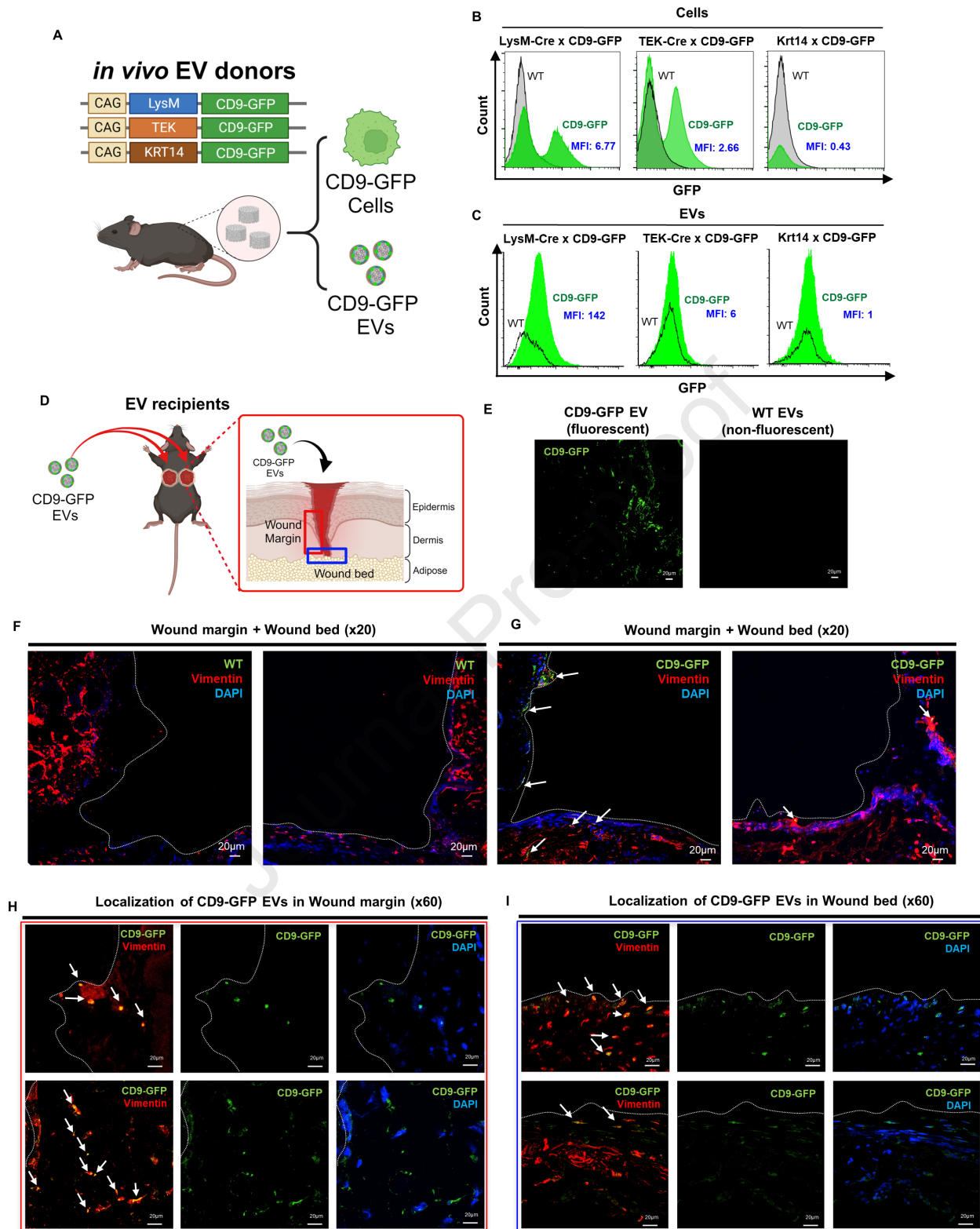
F



G







Eliceiri and colleagues identify a novel intercellular signaling axis mediated by the release of pro-reparative extracellular vesicles from macrophages to accelerate wound healing. We identify biologically active payloads and establish genetic models that define the source and uptake of vesicles into specific cell types in the wound bed.

Journal Pre-proof